A MademoiseLLE domain binding platform
links the key RNA transporter to endosomes

Senthil-Kumar Devan[1, $], Stephan Schott-Verdugo[2, 3, $], Kira Müntjes[1], Lilli Bismar[1], Jens Reiners[4], Eymen Hachani[5], Lutz Schmitt[5], Astrid Höppner[4], Sander HJ Smits[4, 5, *], Holger Gohlke[2, 3, *], Michael Feldbrügge[1, *]

$ shared first authorship

* shared corresponding authorship

[1] Institute of Microbiology, Heinrich Heine University Düsseldorf, Cluster of Excellence on Plant Sciences, 40204 Düsseldorf, Germany

[2] John von Neumann Institute for Computing (NIC), Jülich Supercomputing Centre (JSC), Institute of Biological Information Processing (IBI-7: Structural Bioinformatics), and Institute of Bio- and Geosciences (IBG-4: Bioinformatics), Forschungszentrum Jülich GmbH, Wilhelm-Johnen-Str., 52425 Jülich, Germany

[3] Institute for Pharmaceutical and Medicinal Chemistry, Heinrich Heine University Düsseldorf, 40204 Düsseldorf, Germany

[4] Center for Structural Studies, Heinrich Heine University Düsseldorf, 40204 Düsseldorf, Germany

[5] Institute of Biochemistry I, Heinrich Heine University Düsseldorf, 40204 Düsseldorf, Germany

* **Corresponding authors:**

Dr. Sander HJ Smits

Institute of Biochemistry,

Heinrich Heine University Düsseldorf, 40204 Düsseldorf, Germany

Phone: +49 (211) 81-12647

sander.smits@hhu.de

Dr. Holger Gohlke

Institute for Pharmaceutical and Medicinal Chemistry,

Heinrich Heine University Düsseldorf, 40204 Düsseldorf, Germany

Phone: +49 (211) 81-13662

&

John von Neumann Institute for Computing (NIC), Jülich Supercomputing Centre (JSC), Institute of Biological Information Processing (IBI-7: Structural Bioinformatics), and Institute of Bio- and Geosciences (IBG-4: Bioinformatics), Forschungszentrum Jülich GmbH, 52425 Jülich, Germany

Phone: +49 (2461) 61-85550

gohlke@uni-duesseldorf.de & h.gohlke@fz-juelich.de

Dr. Michael Feldbrügge

Institute of Microbiology,

Bioeconomy Science Center, Cluster of Excellence on Plant Sciences

Heinrich Heine University Düsseldorf, 40204 Düsseldorf, Germany

Phone: +49 (211) 81-15475

feldbrue@hhu.de

1 **Abstract**

2 Spatiotemporal expression can be achieved by transport and translation of mRNAs at defined

3 subcellular sites. An emerging mechanism mediating mRNA trafficking is microtubule-

4 dependent co-transport on shuttling endosomes. Although progress has been made in

5 identifying various components of the endosomal mRNA transport machinery, a mechanistic

6 understanding of how these RNA-binding proteins are connected to endosomes is still lacking.

7 Here, we demonstrate that a flexible MademoiseLLE (MLLE) domain platform within RNA-

8 binding protein Rrm4 of *Ustilago maydis* is crucial for endosomal attachment. Our

9 structure/function analysis uncovered three MLLE domains at the C-terminus of Rrm4 with a

10 functionally defined hierarchy. MLLE3 recognises two PAM2-like sequences of the adaptor

11 protein Upa1 and is essential for endosomal shuttling of Rrm4. MLLE1 and MLLE2 are most

12 likely accessory domains exhibiting a variable binding mode for interaction with currently

13 unknown partners. Thus, endosomal attachment of the mRNA transporter is orchestrated by a

14 sophisticated MLLE domain binding platform.

Devan, Schott-Verdugo *et al.*

Introduction

mRNA localisation and local translation are essential for spatiotemporal control of protein expression. An important mechanism to achieve localised translation is the active transport of mRNAs along the cytoskeleton (Das *et al.*, 2021; Fernandopulle *et al.*, 2021; Mofatteh & Bullock, 2017). Mainly, long-distance transport of mRNA is mediated by motor-dependent movement along microtubules. Transport endosomes are important carriers that move messenger ribonucleoprotein complexes (mRNPs), consisting of RNA-binding proteins and cargo mRNAs on their cytoplasmic surface (Mofatteh & Bullock, 2017; Müntjes *et al.*, 2021; Niessing *et al.*, 2018). This process is evolutionarily conserved in fungi, plants, and animals (Baumann *et al.*, 2012; Cioni *et al.*, 2019; Tian *et al.*, 2020a; Liao *et al.*, 2019; Müntjes *et al..*, 2021; Quentin *et al.*, 2021; Schuhmacher *et al.*, 2021). In endosperm cells of developing rice seeds, cargo mRNAs are transported to the cortical endoplasmic reticulum ER by the action of the two RNA recognition motif (RRM)-containing proteins RBP-P and RBP-L. These form a quaternary complex with membrane trafficking factor NSF (*N*-ethylmaleimide-sensitive factor) and small GTPase Rab5a on the endosomal surface (Tian *et al.*, 2020b). In neurons, mRNA transport has been linked to early and late endosomes as well as lysosomal vesicles. Especially, local translation of mRNAs encoding mitochondrial proteins on the surface of late endosomes is needed for mitochondrial function. Importantly, this trafficking process has been associated with the neuronal Charcot Marie-Tooth disease (Cioni *et al.*, 2019). Annexin 11, a factor implicated in amyotrophic lateral sclerosis (ALS), was found as an mRNP linker on motile lysosomal vesicles (Liao *et al.*, 2019). Also, the five-membered FERRY complex was recently identified connecting mRNAs encoding mitochondrial proteins to neuronal endosomes by interaction with the active form of Rab5 (Quentin *et al.*, 2021; Schuhmacher *et al.*, 2021).

Among the best-studied examples for membrane-coupled mRNA transport is the endosomal mRNA transport in the corn pathogen *Ustilago maydis* (Béthune *et al.*, 2019; Haag *et al.*, 2015; Müntjes *et al.*, 2021). Extensive peripheral movement of mRNAs is needed for efficient unipolar growth of infectious hyphae. These hyphae grow highly polarised by expanding at the growing tip and inserting regularly spaced septa at the basal pole. Loss of mRNA distribution causes aberrant bipolar growth (Baumann *et al.*, 2012; Becht *et al.*, 2006; Pohlmann *et al.*, 2015). Key vehicles of cargo mRNAs are Rab5a-positive endosomes that shuttle along microtubules by the concerted action of plus-end directed kinesin-3 and minus-end directed cytoplasmic dynein (Baumann *et al.*, 2012). Important cargo mRNAs are, for example, all four septin mRNAs. Their local translation during transport is essential to form heteromeric septin complexes on the surface of transport endosomes. Endosomes deliver these

49 complexes to the hyphal tip, forming a defined gradient of septin filaments at the growing pole

50 (Baumann *et al.*, 2014; Olgeiser *et al.*, 2019; Zander *et al.*, 2016).

51   Rrm4 is the key RNA-binding protein of the transport process that recognises defined sets

52 of cargo mRNAs via its three N-terminal RRMs (Fig. 1A; Olgeiser *et al.*, 2019). Rrm4 and

53 bound cargo mRNAs are linked to endosomes by Upa1, containing a FYVE zinc finger for

54 interaction with PI$_3$P lipids (phosphatidylinositol 3-phosphate; Fig 1A; Pohlmann *et al.*, 2015;

55 Stenmark *et al.*, 2002). The adaptor protein Upa1 contains a PAM2 motif (poly[A]-binding

56 protein interacting motif 2; Albrecht & Lengauer, 2004; Jinek *et al.*, 2010; Kozlov *et al.*, 2004)

57 and two PAM2-like (PAM2L) sequences. These motifs are crucial for interaction with

58 MademoiseLLE (MLLE) domains of the poly(A)-binding protein Pab1 and Rrm4, respectively

59 (Fig. 1A; Pohlmann *et al.*, 2015).

60   The MLLE domain was first identified as a conserved domain at the C-terminus of the

61 human cytoplasmic poly(A)-binding protein 1 (PABP1C; Mangus *et al.*, 1998; Mangus *et al.*,

62 2003). Solution and crystal structures of PABC domains from PABP1C and ubiquitin ligase

63 UBR5 showed that they are structurally conserved (Deo *et al.*, 2001; Kozlov *et al.*, 2001). The

64 domain is about 70 amino acids in length and consists of five bundled α-helices. Interaction

65 with the PAM2-binding motif (consensus sequence xxLNxxAxEFxP) is characterised by the

66 central α-helix 3 with the sequence KITG<u>MLLE</u> and mediated by two adjacent hydrophobic

67 pockets (Xie *et al.*, 2014), with the binding of the Phe residue of the PAM2 motif being the

68 major determinant for this interaction (Kozlov & Gehring, 2010). Besides human PABPC1,

69 there are currently only two additional proteins with MLLE domains described: the ubiquitin

70 ligase UBR5 functioning, for example, during microRNA-mediated gene silencing (Su *et al.*,

71 2011) and Rrm4-type RNA-binding proteins from fungi (Fig. 1B; Müller *et al.*, 2019).

72   Mutations in the C-terminal MLLE domain of Rrm4 result in the loss of Rrm4 motility,

73 suggesting that the link to endosomes is disrupted (Becht *et al.*, 2006). Consistently, the C-

74 terminus of Rrm4 recognises the PAM2L sequence of the adaptor protein Upa1 (Pohlmann *et*

75 *al.*, 2015), suggesting that the interaction of MLLE domains with PAM2L sequences is

76 responsible for its endosome association. This study combines structural biology with fungal

77 genetics to demonstrate that the C-terminal half of Rrm4 has three divergent MLLE domains

78 with a flexible arrangement and each domain contributes differentially to the endosomal

79 attachment.

80

81   **Results**

82   **Iterative structural modelling predicts three MLLE domains at the C-terminus of Rrm4**

83   To generate structural models of the MLLE domains present in Rrm4, we focused on the C-
84   terminal part of the protein (residues 421 to 792). This excluded the three N-terminal RRMs
85   but included the previously predicted two C-terminal MLLE domains (Fig. 1A-B; Müller *et al.*,
86   2019). Subjecting this Rrm4 sequence region to iterative comparative modelling with
87   TopModel (Fig. 1C; Mulnaes *et al.*, 2020a) revealed, as expected, the previously identified two
88   regions with homology for MLLE domains located at residues 571-629 and 712-791 (denoted
89   MLLE2 and MLLE3; Fig. 1C; Müller *et al.*, 2019). Unexpectedly, using the TopModel
90   workflow with its efficient template selection capabilities (Mulnaes *et al.*, 2020a), we identified
91   an additional *de novo* predicted MLLE domain located at residues 451-529 (denoted MLLE1;
92   Fig. 1B-C; Fig. EV1A). Although the sequence identity between templates and their respective
93   Rrm4 sequence stretches is only 17 to 32% (Fig. 1B, Fig. EV1A), the generated MLLE domain
94   models have a high predicted local structural quality, as assessed by TopScore (Fig. 1C;
95   Mulnaes & Gohlke, 2018). The generated models were also verified by the current deep neural
96   network modelling approaches AlphaFold2 and RoseTTAFold (Fig. EV1B; Baek *et al.*, 2021;
97   Jumper *et al.*, 2021), further indicating that the C-terminal half of Rrm4 has three MLLE
98   domains instead of the previously identified two. All of these MLLE domains might be relevant
99   for the interaction with Upa1.

100   **X-ray analysis of the second MLLE domain confirms the predicted structural models**

101   To verify the structural models further, we expressed and purified an N-terminally truncated
102   version of the Rrm4 carrying the three MLLE domains in *Escherichia coli* (Fig. EV2A-B;
103   version H-Rrm4-NT4 carrying an N-terminal hexa-histidine-tag; Pohlmann *et al.*, 2015;
104   Materials and methods). Size exclusion chromatography combined with Multi-angle light
105   scattering (MALS) indicates that the protein is homogenous and does not form aggregates (Fig.
106   EV2C). We thus set out to crystallize the protein for X-ray diffraction analysis (see Material
107   and Methods). Testing 2016 different conditions, crystals were only obtained in individual
108   cases after at least 7 days of incubation. A complete dataset was collected from a single crystal
109   diffracting to 2.6 Å resolution and a $P4_32_12$ symmetry. Data and refinement statistics are given
110   in Appendix Table S2. Surprisingly, the unit cell dimensions were small and, with a Matthews
111   coefficient assuming 50% solvent content, only 128 amino acids would fit into the asymmetric
112   unit of the crystal. Hence, the unit cell has an insufficient size to cover H-Rrm4-NT4, which

113   contains 380 amino acids. Using the predicted models of MLLE1-3 as templates for molecular

114   replacement, only MLLE2 gave a clear solution, showing after refinement that two copies of

115   MLLE2 (residues 567-630) were present in the asymmetric unit. For comparison, previously,

116   two copies of the MLLE domain in the asymmetric unit were reported in crystals of MLLE of

117   UBR5 (Munoz-Escobar *et al.*, 2015). The structural data indicates that the protein was truncated

118   from both termini during crystallisation, resulting in a shortened version of the H-Rrm4-NT4

119   protein that formed stable crystals (see Material and methods). Both MLLE2^{Rrm4} copies adopt

120   the same overall fold as seen by the RMSD of 0.29 Å over 59 C-alpha atoms. The MLLE2^{Rrm4}

121   crystal structure displays high similarity with the MLLE domain of the ubiquitin ligase UBR5

122   (MLLE^{UBR5}; Munoz-Escobar *et al.*, 2015; PDB code 3NTW, RMSD of 0.97 Å over 56 amino

123   acids) and the MLLE domain of PABPC1 (Kozlov *et al.*, 2010; PDB code 3KUS, RMSD of

124   1.34 Å over 61 amino acids). The MLLE2^{Rrm4} domain consists of four helices (designated α2 -

125   5; Fig. 2A) arranged as a right-handed superhelix similar to MLLE^{UBR5}. In comparison to the

126   MLLE domain of PABPC1, the first short helix is absent in both MLLE2^{Rrm4} and MLLE^{UBR5}

127   structures.

128   When comparing the obtained crystal structure with the MLLE2^{Rrm4} model generated by

129   TopModel, the average RMSD is 0.62 Å over the backbone atoms, close to the uncertainty of

130   the atomic coordinates of the experimental structure (Fig. 2B). Importantly, this confirms our

131   structural model of MLLE2^{Rrm4} and strongly suggests that the modelled MLLE1^{Rrm4} and

132   MLLE3^{Rrm4} domains should be of equally high quality.

133   We compared the predicted models of MLLE1-3^{Rrm4} with the known structure of the human

134   PABPC1 focusing on the well-described PAM2 peptide-binding pocket. This revealed that

135   MLLE3^{Rrm4} maintains a characteristic Gly residue at position 736 that binds the conserved Phe

136   residue of the PAM2 motifs, a major binding determinant in PABPC1 and UBR5 (Kozlov &

137   Gehring, 2010; Munoz-Escobar *et al.*, 2015; Fig. 2C). However, the binding interfaces of

138   MLLE1^{Rrm4} and MLLE2^{Rrm4} are altered compared to the 'canonical' binding site in PABPC1

139   and UBR5 (Fig. 2C). Instead of Gly, MLLE1^{Rrm4} and MLLE2^{Rrm4} have a Ser and Arg in the

140   corresponding positions 471 and 573. The notion that MLLE1^{Rrm4} and MLLE2^{Rrm4} may differ

141   from canonical MLLE domains is also supported by the lower sequence identity of MLLE1^{Rrm4}

142   and MLLE2^{Rrm4} when compared to previously characterised MLLE domains (Fig. 1B; EV1A).

143   In summary, structural modelling revealed the presence of three MLLE domains at the C-

144   terminus of Rrm4. Furthermore, the structure of the MLLE2^{Rrm4} domain was successfully

145   verified by X-ray crystallographic analysis. MLLE1^{Rrm4} and MLLE2^{Rrm4} are divergent in the

146 key region of PAM2 binding, suggesting that these domains might employ a different binding

147 mode or show a different binding specificity.

The MLLE domains of Rrm4 form a binding platform with flexible arrangement of the

149 **individual domains**

150 To study the relative arrangement of all three MLLE^{Rrm4} domains and the orientation to the N-

151 terminal RRMs, we performed Small-Angle X-ray Scattering (SAXS) experiments. We

152 expressed and purified H-Rrm4-NT4 as well as the full-length protein with N-terminal GST

153 fusion (glutathione S-transferase; G-Rrm4) from *E. coli* (see Materials and methods). Primary

154 data analysis of the scattering curves (Tria *et al.*, 2015; Konarev *et al.*, 2003) revealed that both

155 proteins are monomeric and highly flexible in solution (Appendix Table S3; Fig. 2D-E; Fig.

156 EV2D-E). To visualise the different protein conformations, we performed an Ensemble

157 Optimization Method (EOM) analysis for both the G-Rrm4 and H-Rrm4-NT4 proteins (Fig 2D-

158 E). We used our MLLE models and a GST model (PDB entry: 1ua5) together with the protein

159 sequence for G-Rrm4 as input, yielding a distribution of different conformations of the protein

160 in solution (representative models in Fig. EV2E). One model of G-Rrm4, representing 25% of

161 the population, revealed that the C-terminal part containing MLLE1-3^{Rrm4} adopts an elongated

162 and mainly unfolded but open conformation (Fig. 2D; Fig. EV2D-E). The N-terminal part,

163 containing RRM domains of the GST fusion protein, adopts a more globular structure,

164 indicating less flexibility within this region (Fig. 2D; Fig. EV2D-E). Studying only the C-

165 terminal part of Rrm4 revealed that the most prominent model of this analysis (75 % of the

166 population) has a nearly identical conformation as the one selected for G-Rrm4 (Fig. 2D-E, Fig.

167 EV2E). It suggests that the C- terminal part of Rrm4-NT4 adopts a very similar orientation

168 when expressed by itself. This analysis deduces that the MLLE1-3^{Rrm4} domains form a C-

169 terminal binding platform with a flexible arrangement for multiple contact sites for binding

170 partners. Thus, the RRM domains for RNA interaction is spatially separated from the protein

171 interaction platform.

The third MLLE is essential for interaction with PAM2 like sequences of Upa1

173 To evaluate the interaction capacity of MLLE1-3^{Rrm4}, we performed *in vitro* binding studies.

174 We expressed different deletion versions of Rrm4 as N-terminal GST fusions in *E. coli*. As a

175 control, we expressed an N-terminal GST fusion of the MLLE domain of Pab1 (Fig. 3A;

176 Materials and methods). To check the physical interaction with PAM2 and PAM2L sequences

177 of Upa1, we expressed 18 amino acid fragments (Fig. 3A) as N-terminal hexa-histidine-SUMO

178 (HS) fusion proteins (see Materials and methods). In GST pull-down experiments using GST

179 fusion proteins as bait, G-Pab1-MLLE interacts with HS-PAM2 but not with the HS-PAM2L

180 motifs of Upa1 (Fig. EV3B, lane 2). Conversely, G-Rrm4-NT4 recognises the two HS-PAM2L

181 motifs of Upa1 but not the HS-PAM2 motif (Fig. EV3B, lane 3; Pohlmann *et al.*, 2015).

182 Interestingly, the interaction with both PAM2L motifs was lost when MLLE3^{Rrm4} was deleted

183 (G-Rrm4-NT4-M3Δ; Fig. EV3B, lane 6), while constructs with deletion of MLLE1^{Rrm4} or

184 MLLE2^{Rrm4}, or both MLLE1^{Rrm4} and MLLE2^{Rrm4}, still interacted with the HS-PAM2L motifs

185 of Upa1 (Fig. EV3B, lane 4,5 and 7).

186 To validate qualitatively whether these results also hold true for full-length proteins, we

187 performed yeast two-hybrid experiments comparable to previous studies (Pohlmann *et al.*,

188 2015). To this end, Upa1 or Rrm4 versions were fused at the N-terminus with the DNA-binding

189 domain (BD) and activation domain (AD) of Gal4p, respectively (see Materials and methods;

190 the C-termini were fused with the enhanced version of the green fluorescent protein [Gfp],

191 Clontech; or the monomeric version of red fluorescent protein mKate2 [Kat], respectively;

192 Müntjes *et al.*, 2020; Pohlmann *et al.*, 2015). Rrm4-Kat interacts with full-length Upa1-Gfp

193 (Fig. EV3C, Pohlmann *et al.*, 2015) and interaction was lost when MLLE3^{Rrm4} was deleted.

194 Mutations in MLLE1^{Rrm4}, MLLE2^{Rrm4} or MLLE1,2^{Rrm4} did not alter the interaction with Upa1-

195 Gfp (Fig. EV3C). To further investigate the presence of unknown interaction motifs in Upa1-

196 Gfp, variants carrying block mutations in either or both PAM2L1 and PAM2L2 motifs were

197 tested against the Rrm4-Kat versions (Fig. EV3C). Upa1-Gfp versions with block mutations in

198 either PAM2L1 or PAM2L2 still interact with the Rrm4-Kat versions (Fig. EV3C). However,

199 when both PAM2L1,2 motifs were mutated, the interaction between the Upa1 and Rrm4 is lost,

200 comparable to earlier observation (Fig. EVC; Pohlmann *et al.*, 2015). Invariably, MLLE3^{Rrm4}

201 deletion caused loss of interaction with all Upa1-Gfp versions (Fig. EV3C). These results

202 confirm that the MLLE3^{Rrm4} domain is essential for the interaction with Upa1. MLLE1^{Rrm4} and

203 MLLE2^{Rrm4} appear to be dispensable for the interaction with Upa1 suggesting the presence of

204 additional interaction partners (see below).

205 To obtain quantitative data on the protein/peptide interactions, we performed isothermal

206 titration calorimetry (ITC) experiments with purified proteins (Fig. EV3D) and synthetic

207 peptides with a length of 18 amino acids (PAM2^{Upa1}, PAM2L1^{Upa1}, and PAM2L2^{Upa1}; Fig. 3A).

208 The binding constant K_D and the binding stoichiometry was calculated from the curves, which

209 in all cases indicated a 1:1 ratio between the G-Rrm4-NT4 protein and the binding partner.

210 Testing G-Pab1-MLLE with the peptides revealed a K_D of 14.6 μM for PAM2^{Upa1} (Fig.

211 EV3D), which is within the range of observed K_D of 0.2 to 40 μM for known MLLE/PAM2

212 interactions like the MLLE domain of PABPC1 with various PAM2 sequences (Mattijssen *et*

213   *al.*, 2021). Testing G-Pab1-MLLE with PAM2L1[Upa1] and PAM2L2[Upa1] peptides, no indication

214   for binding was observed. PAM2L sequences are rich in acidic residues and exhibit a different

215   FxxP spacing than the canonical FxP sequence of PAM2 sequences in the core region (Fig. 3A,

216   EV3D; see Discussion). The observed binding behaviour indicates a clear binding specificity

217   differentiating PAM2 and PAM2L peptides. This is in line with the previously published GST

218   pull-down experiments (Pohlmann *et al.*, 2015).

219   In comparison, testing G-Rrm4-NT4 with the peptides revealed a K_D of 14.9 μM for

220   PAM2L1[Upa1] and 5.1 μM for PAM2L2[Upa1] and no binding to PAM2[Upa1] (Fig. 3B). This suggests

221   a similar affinity when compared to the interactions of MLLE[Pab1] with PAM2 and demonstrates

222   the high sequence specificity of the MLLE domains to their respective PAM2L sequences (see

223   Discussion).

224   Analysing G-Rrm4-NT4-M3Δ with a deletion of MLLE3[Rrm4] revealed that binding to

225   PAM2L1[Upa1] and PAM2L2[Upa1] was no longer detectable (Fig. 3C). This is in line with

226   observations from the GST pull-down experiments (Fig. EV3B). This suggests that MLLE3[Rrm4]

227   is essential for binding. Testing G-Rrm4-NT4 versions carrying deletions in either MLLE1[Rrm4]

228   or MLLE2[Rrm4] showed no difference in binding affinity (Fig. EV3F-G). Even testing G-Rrm4-

229   NT4 with a deletion in both MLLE1,2 domains deleted exhibited a binding affinity in the same

230   range as the wild type version containing all three MLLEs (Fig. 3D). We conclude that (i)

231   MLLE3[Rrm4] is vital for recognising PAM2L sequences with a higher affinity to PAM2L2 and

232   (ii) neither MLLE1[Rrm4] nor MLLE2[Rrm4] contribute to the binding of PAM2L or PAM2 motifs

233   (Fig. EV3H-I, see Materials and methods). This is consistent with our structural analysis

234   revealing a differences in the binding site for these MLLE domains (see Discussion).

235

236   **The third MLLE domain of Rrm4 is essential for its function**

237   To address how the different MLLE domains contribute to the biological function of Rrm4, we

238   generated *U. maydis* strains carrying deletions in the respective domains of Rrm4 (Fig. 4A). As

239   genetic background, we used laboratory strain AB33, expressing the heteromeric master

240   transcription factor of hyphal growth (bE/bW) under control of the nitrate inducible promoter

241   P*nar1*. Thereby, polar hyphal growth can be elicited efficiently and in a highly reproducible

242   fashion by changing the nitrogen source (Fig. 4B, top; Brachmann *et al.*, 2001). To investigate

243   dynamic endosomal transport, we used strains expressing functional C-terminal fusion Upa1-

244   Gfp and Rrm4-Kat (see Materials and methods).

9

245   The resulting hyphae grew with a defined axis of polarity, i.e., they expanded at the hyphal

246   tip and inserted basal septa leading to the formation of empty sections (Fig. 4B-C). Loss of

247   Rrm4 (*rrm4Δ* strain) caused the formation of hyphae growing at both ends, characteristic for

248   aberrant bipolar growth (Fig. 4B-C; Pohlmann *et al.*, 2015). Testing Rrm4-Kat versions

249   carrying deletions of MLLE1^{Rrm4} or MLLE2^{Rrm4} did not cause alterations in unipolar growth

250   (Fig. 4B-C). Furthermore, endosomal shuttling and co-localisation were indistinguishable from

251   wild type (Fig. 4D-E). Also, the number of endosomes (number of signals / 10 μm, Fig. EV4A),

252   velocity, and processivity (Fig. EV4B-C) were comparable to wild type. Hence, the first two

253   MLLE domains were dispensable for polar growth and endosomal shuttling under optimal

254   growth conditions. Since the deletion of the first two MLLEs did not substantially alter the

255   function of Rrm4, we can infer that the deletion neither affects the overall structure of the

256   protein nor interfere with other domains like the RNA-binding domain of the protein. This

257   supports the conclusions of our biochemical experiments (see above).

258   Importantly, testing strains expressing Rrm4-Kat with deletion of the third MLLE domain

259   revealed a loss-of-function phenotype similar to *rrm4Δ* strains. The number of bipolar hyphae

260   was comparable to *rrm4Δ* strains (Fig. 4B-C; mutation identical to allele *rrm4G^{PΔ}* in Becht *et*

261   *al.*, 2006). We observed drastic alteration in shuttling, and Rrm4 aggregates did not co-localise

262   with motile Upa1-positive signals (Fig. 4D-E). While the Rrm4 signals were static (Fig. 4D-E;

263   Fig. EV4A-C), the number of motile Upa1-Gfp positive endosomes, their velocity, and their

264   processivity were not affected (Fig. EV4A-C, summarised in Fig. EV4D). This is consistent

265   with previous results showing that the third MLLE domain is important for the movement of

266   Rrm4 and that endosomal shuttling of Upa1 is not affected if Rrm4 is missing (Baumann *et al.*,

267   2012; Becht *et al.*, 2006; Pohlmann *et al.*, 2015). To conclude, MLLE3^{Rrm4} is an essential

268   domain for Rrm4 attachment to endosomes in contrast to MLLE1 and MLLE2^{Rrm4}.

269

The second MLLE domain plays accessory roles in endosomal Rrm4 attachment

270

271   To investigate the biological role of MLLE1^{Rrm4} and MLLE2^{Rrm4} in more detail, we generated

272   strains expressing Rrm4-M1,2Δ-Kat, lacking both MLLE1^{Rrm4} and MLLE2^{Rrm4} domains, and

273   tested the influence on hyphal growth. Unipolar growth was not disturbed (Fig. 5A-B). To

274   challenge the endosomal attachment of Rrm4, we expressed Upa1-Gfp versions carrying

275   mutations in PAM2L motif 1 or 2 as well as in both motifs; these motifs are important for Rrm4

276   interaction (Fig. 4A; Pohlmann *et al.*, 2015). Strains expressing Rrm4-M1,2Δ-Kat in

277   combination with mutated PAM2L1 or PAM2L2 of Upa1 showed unipolar growth comparable

278   to wild type (Fig. 5A-B; Fig. EV5A-B), indicating that MLLE1^{Rrm4} and MLLE2^{Rrm4} are

279   dispensable for unipolar growth even when the endosomal attachment was weakened by

280   expressing Upa1 versions with mutated PAM2L motifs (Fig. EV4D). When studying Upa1

281   mutated in both PAM2L motifs, we observed an aberrant bipolar growth phenotype comparable

282   to the *upa1Δ* strain (Fig. 5A-B). This was expected, since the interaction of Rrm4 to endosomes

283   is mediated by both PAM2L motifs (Pohlmann *et al.*, 2015). Analysing Rrm4-M1,2Δ-Kat in

284   this genetic background revealed no additive phenotype (Fig. 5A-B). This reinforces that the

285   interactions of PAM2L motifs of Upa1 are the major determinants for endosomal attachment

286   of Rrm4.

287   Next, we investigated endosomal shuttling. In strains expressing Rrm4-M1,2Δ-Kat missing

288   MLLE1^{Rrm4} and MLLE2^{Rrm4} endosomal shuttling was not disturbed (Fig. 5C). The number of

289   motile Rrm4-M1,2Δ-Kat positive signals, their velocity, and their processivity were not

290   affected (Fig. EV5C-D). Like above, we challenged the endosomal attachment of Rrm4 by

291   expressing Upa1 versions with mutations in the PAM2L motifs. As expected, simultaneous

292   mutation of both PAM2L motifs of Upa1 resulted in a reduction in the number of Rrm4-Kat

293   positive shuttling endosomes (Fig. 5C, EV5E; Pohlmann *et al.*, 2015). When both PAM2L

294   motifs were mutated, the Rrm4-Kat version is misloclised and aberrantly attached to

295   microtubules (MT) in about 80% of hyphae (Fig. 5C-D). This mislocalisation is a characteristic

296   feature for altered endosomal attachment of Rrm4 due to the accumulation of static Rrm4-Kat,

297   which can be also seen in *upa1Δ* strains (Fig. EV5C; Jankowski *et al.*, 2019). Quantifiying

298   Rrm4-Kat signals exhibiting processive movement in kymographs revealed that strains

299   exhibiting aberrant microtubule staining resulted in reduced fluorescence (Fig. 5E) indicating

300   fewer Rrm4-Kat versions on shuttling endosomes. As an important control, we treated the

301   strains with the microtubule inhibitor benomyl, demonstrating aberrant staining is microtubule-

302   dependent (Fig. EV5F). Furthermore, Western blot analysis demonstrated that mutations in

303   Rrm4 do not alter the protein amount (Fig. EV5G). Comparable to previous reports, we

304   observed residual motility of Rrm4-Kat on shuttling endosomes if both PAM2L motifs are

305   mutated or if *upa1* is deleted (Fig. 5C). This indicates additional proteins besides Upa1 are

306   involved in the endosomal attachment of Rrm4 (Pohlmann *et al.*, 2015).

307   To analyse the influence of individual PAM2L motifs, we determined the number of

308   hyphae with aberrant microtubule staining in strains co-expressing Rrm4-Kat versions and an

309   Upa1-Gfp version with mutations of PAM2L sequence 1 or 2. Mutations in PAM2L1 and

310   PAM2L2 causes 8% and 19% of hyphae with aberrant MT staining, respectively (Fig. 5D).

311   Hence, the interaction of PAM2L2 is more important for correct endosomal attachment of

312   Rrm4. This is consistent with our biochemical results demonstrating that MLLE3[Rrm4] binds

313   stronger to PAM2L2 of Upa1 than to PAM2L1 (Fig. 3D).

314   Next, we investigated the association of Rrm4-M1,2Δ-Kat in strains expressing Upa1 with

315   mutated PAM2L1. In this strain, the endosomal attachment was solely dependent on the

316   interaction of MLLE3[Rrm4] with the PAM2L2 sequence of Upa1. We did observe 6% of hyphae

317   with aberrant MT staining (Fig. 5D; Fig. EV4D). This was comparable to strains expressing

318   Rrm4-Kat, suggesting no clear difference (Fig. 5D). However, testing Upa1 with its PAM2L2

319   mutated, leaving only PAM2L1 for interaction with Rrm4, we observed a clear increase in

320   hyphae with aberrant MT staining when comparing strains co-expressing Rrm4-M1,2Δ-Kat

321   versus Rrm4-Kat (52% versus 19%; Fig. 5D-E). Hence, the region covering MLLE1[Rrm4] and

322   MLLE2[Rrm4] was important for Rrm4 attachment. Finally, we tested individual deletions in

323   MLLE1[Rrm4] and MLLE2[Rrm4] in combination with mutated PAM2L2 in Upa1 to dissect the role

324   of the different MLLE domains. In strains expressing Rrm4-Kat or Rrm4-M1Δ-Kat with this

325   type of Upa1 mutation, the number of hyphae with aberrant MT staining was comparable (18%

326   versus 11%, respectively; Fig. 5D). However, strains expressing Rrm4-M2Δ-Kat exhibited an

327   increased number of hyphae with aberrant MT staining that was comparable to Rrm4-M1,2Δ-

328   kat (51% versus 52% respectively; Fig. 5D; Fig. EV4D). As mentioned above, aberrant MT

329   localisation of mutated Rrm4-M2Δ-Kat and Rrm4-M1,2Δ-Kat also exhibited reduced intensity

330   of processive signals in Rrm4 kymographs (Fig. 5E) suggesting that the endosomal association

331   was altered. To conclude, for MLLE1[Rrm4] we were unable to assign a clear function yet.

332   However, MLLE2[Rrm4] plays an accessory role in the endosomal attachment of Rrm4. In

333   essence, the C-terminus of Rrm4 contains three MLLE domains, with MLLE2[Rrm4] fulfilling an

334   accessory role and MLLE3[Rrm4] having an essential function during the attachment of mRNPs

335   to endosomes.

336

337   **Discussion**

338   Combining structural biology and biophysical techniques with fungal genetics and cell biology,

339   we addressed how mRNPs can be mechanistically linked to endosomes in the model fungus *U.*

340   *maydis*. Previously, it was found that the C-terminal MLLE domain of Rrm4 is needed for

341   shuttling (Becht *et al.*, 2006) and that the C-terminus of Rrm4 interacts with two PAM2L motifs

342   of Upa1 (Pohlmann *et al.*, 2015). Now, we demonstrate that this region of Rrm4 contains not

343   only two MLLE domains, but a sophisticated binding platform consisting of three MLLE

344   domains with MLLE2 and MLLE3 functioning in linking the key RNA transporter to

345   endosomes. We disclose a strict hierarchy with main and accessory domain. The accessory

346   MLLE2 domain shows variations in the critical region of the predicted PAM2 binding pocket,

347   suggesting a novel mode of interaction with currently unknown interaction partners. Rrm4

348   represents the first protein containing multiple MLLE domains to form a binding platform to

349   the best of our knowledge. This interaction unit is essential for the correct endosomal

350   attachment and, hence, mRNP trafficking.

351   **The MLLE / PAM2 connection**

352   The founding member of the MLLE domain family is present at the C-terminus of the poly(A)-

353   binding protein PABPC1. This domain interacts with PAM2 motifs of numerous interaction

354   partners such as GW182, eRF3, and the RNA-binding protein LARP4 functioning in

355   microRNA biology, translational termination, and posttranscriptional control, respectively

356   (Jinek *et al.*, 2010; Kozlov & Gehring, 2010; Yang *et al.*, 2011). Structural analysis revealed a

357   common mode of binding, where the Leu and particularly the Phe of the PAM2 consensus motif

358   xx<u>L</u>NxxAxE<u>F</u>xP (Fig. EV3A) are interacting with helix 2 and 3 as well as helix 3 and 5 of

359   MLLE domain, respectively (Kozlov & Gehring, 2010; Xie *et al.*, 2014). Indeed, the interaction

360   of MLLE with a hydrophobic amino acid is highly conserved, which in most cases is Phe with

361   a known exception in the variant PAM2w motif of LARP4 and LARP4A, where Trp is found

362   (Fig. EV3A; Grimm *et al.*, 2020; Yang *et al.*, 2011; Xie *et al.*, 2014).

363   Studying the MLLE domain-containing protein Rrm4, we discover that it has three MLLE

364   domains in its C-terminal half. MLLE3[Rrm4] binds PAM2L motifs of Upa1 with a K_D of 5 and

365   15 μM for PAM2L2[Upa1] and PAM2L1[Upa1], respectively. The binding affinities are in the same

366   range as described for other MLLE/PAM2 interactions: for example, the binding of

367   MLLE[PABPC1] with PAM2[LARP1], PAM2[Tob2-125], PAM2[LARP4] exhibit a K_D of 3.8, 16 and 22 μM,

368   respectively (Mattijssen *et al.*, 2021). Importantly, our biophysical assessment confirms the

369   exquisite binding specificity of MLLE[Rrm4] that recognises PAM2L1[Upa1] and PAM2L2[Upa1] but

370   not the PAM2[Upa1] version. PAM2L sequences contain a stretch of acidic amino acids in the N-

371   terminal half, and the spacing of FxxP in the core sequence is altered (Fig. EV3A). These

372   variations might account for the differential binding mode. Visual inspection of the potential

373   PAM2L binding region in the predicted model revealed that MLLE3[Rrm4] contains a Gly at

374   position 736 to sustain the binding of an aromatic residue of PAM2L as described for other

375   MLLE domains (see above). However, we were unable to uncover the structural basis for the

376   sequence specificity. Towards this end, future structural studies are required to provide detailed

377   information on the interaction of MLLE3[Rrm4] with PAM2L sequences.

378   Differential PAM2 binding has also been described for the MLLE[UBR5]. This MLLE domain
379   interacts with PAM2[PAIP] with an affinity of 3.4 µM (Lim *et al.*, 2006), whereas it binds a
380   PAM2L sequence (Fig. EV3A) in its own HECT domain with lower affinity (K_D of 50 µM).
381   The latter interaction has been implicated in regulating the HECT ligase activity (Munoz-
382   Escobar *et al.*, 2015). Interestingly, the PAM2L sequence within the HECT domain of UBR5
383   is highly similar to the PAM2L1 and -2 of Rrm4: (i) the sequences contain an acidic stretch N-
384   terminal to the conserved Phe (Fig. EV3A), (ii) the distance between Phe and Pro is two instead
385   of one amino acid, and (iii) the PAM2L sequence contains an additional bulky Tyr in close
386   vicinity to the Phe residue. Remarkably, MLLE[PABC1] does not recognise the PAM2L sequence
387   of UBR5 (Munoz-Escobar *et al.*, 2015). In essence, although the strong sequence specificity of
388   MLLE[Rrm4] and MLLE[Pab1] from *U. maydis* is, to the best of our knowledge, so far unique, we
389   hypothesise that differential PAM2 and PAM2L interactions are evolutionarily conserved and
390   might be more widespread than currently anticipated.
391   We also observed a clear binding specificity for MLLE[Pab1] from *U. maydis* that interacts
392   with PAM2[Upa1] but not the PAM2L sequences from Upa1 (Fig. 6). MLLE[Pab1] binds with
393   comparable affinity to the PAM2[Upa1] (K_D of about 14 µM, Fig EV3E). Previously, we showed
394   that mutations in PAM2[Upa1] strongly decreased MLLE[Pab1] binding but did not interfere with the
395   endosomal shuttling of Pab1 (Pohlmann *et al.*, 2015). Thus, there might be other members of
396   the endosomal mRNPs interacting with Pab1 and stabilising its endosomal association. In fact,
397   the dimerising scaffold protein Upa2 of endosomal mRNA transport contains four PAM2
398   motifs offering eight potential PAM2 motifs for interaction with Pab1 (Fig. 6). However,
399   mutating all four PAM2 motifs did not interfere with endosomal mRNA transport, although
400   interaction with MLLE[Pab1] was lost (Jankowski *et al.*, 2019), confirming a potential redundancy.
401   Consistently, mutations in PAM2 of human LARP4B did not interfere with the function of
402   stress granule recruitment, suggesting additional factors in this case (Grimm *et al.*, 2020).
403   Studying the other two MLLE domains of Rrm4 revealed that both lack the canonical Gly
404   for interactions with PAM2 or PAM2L sequences. MLLE1[Rrm4] and MLLE2[Rrm4] have Ser471
405   and Arg573 instead, respectively. Consistently, MLLE1[Rrm4] and MLLE2[Rrm4] do not bind PAM2
406   or PAM2L sequences. Thus, although the general fold of the MLLE domain is probably
407   conserved in MLLE1[Rrm4] and MLLE2[Rrm4], these domains most likely exhibit a different binding
408   specificity to their potential protein partner. Our detailed *in vivo* analysis revealed that MLLE2
409   carries out an accessory function for the correct attachment of Rrm4 during endosomal
410   shuttling. In the case of MLLE1 we did not identify a clear function so far. However, we believe
411   that all three MLLE domains are functionally important. This is supported by the fact that the

14

412 presence of an MLLE binding platform with three MLLE domains is evolutionarily conserved.

413 Even Rrm4 versions of the distantly related fungus *Rhizophagus irregularis* contains three

414 MLLE domains (Mucoromycota, determined by AlphaFold; Müller *et al.*, 2019).

415   Studying the spatial arrangement of the three MLLE domains revealed that they form a

416 highly flexible binding platform pertinent for the regulation of Rrm4 mRNP transport. This

417 would allow for the simultaneous interaction of several binding partners and potential

418 rearrangements like an induced fit after binding. Such a scenario might be crucial during the

419 loading and unloading of mRNPs to endosomes. Noteworthy, the N-terminal RNA-binding

420 domain consisting of three RRMs is clearly separated from the MLLE domains for endosomal

421 attachment. This is comparable with the arrangement of RRM and MLLE domains in human

422 PABPC1: the four N-terminal RRM domains interact with the poly(A) tail of mRNAs, and a

423 flexible spacer region exposes the MLLE domain for protein/protein interactions (Schäfer *et*

424 *al.*, 2019). Within the spacer region, additional interactions with the RRM2 of PABPC1 were

425 found, suggesting a function in multimerization of the protein on the poly(A) tail of mRNAs

426 (Sawazaki *et al.*, 2018).

427 **Conclusion**

428 Endosomal mRNA transport is evolutionarily highly conserved. Besides hyphal growth in

429 fungi, it is important for endosperm development in plants as well as neuronal functions in

430 animals and humans (Béthune *et al.*, 2019; Fernandopulle *et al.*, 2021; Müntjes *et al.*, 2021;

431 Tian *et al.*, 2020a). Malfunctioning of this process causes defects in polar growth in fungi and

432 has been implicated in neuronal diseases such as Charcot-Marie-Tooth type 2B neuropathy or

433 amyotrophic lateral sclerosis in humans (Cioni *et al.*, 2019; Liao *et al.*, 2019).

434 A key question is how mRNPs are linked to endosomes. In plants, two RRM-type RNA-binding

435 proteins form a complex with cargo mRNAs and the endosomal component *N*-ethylmaleimide-

436 sensitive factor NSF as well as Rab5a (Tian *et al.*, 2018; Tian *et al.*, 2020a; Tian *et al.*, 2020b).

437 Comparably, the FERRY complex (Five-subunit Endosomal Rab5 and RNA/ribosome

438 intermediarY) interacts with the activated GTP-bound form of Rab5 during endosomal mRNA

439 transport in neurons (Schuhmacher *et al.*, 2021; Quentin *et al.*, 2021). Further examples are the

440 membrane-associated protein Annexin 11 that links large RNA granules to lysosomal vesicles

441 during mRNA transport in neuronal axons and dendrites (Liao *et al.*, 2019). Thus, a number of

442 components and interactions are known, however detailed structural insights are scarce. Here,

443 we have demonstrated that in hyphae, endosomal attachment of Rrm4 is mediated by an MLLE

444 binding platform with a non-canonical accessory domain joining an essential MLLE domain

445   for perfect interaction to Upa1 on the endosomal surface (Fig. 6). This binary interaction in the

446   core of the transport mRNPs is supported by numerous interactions of additional protein

447   partners such as Upa2 and Pab1 that assist in attaching components to the endosomal surfaces

448   (Fig. 6). In closing, studying endosomal mRNP transport in fungal model systems might guide

449   future research endeavours in plant and neuronal systems.

450   **Materials and methods**

451   **Structural modelling of C-terminal MLLE domains of Rrm4**

452   To obtain structural models of the C-terminal region of Rrm4, an iterative homology modelling

453   approach was used with the TopModel workflow (Mulnaes *et al.*, 2020a). Initially, the entire

454   C-terminal region (421 to 792) was submitted as input in TopModel and identified templates

455   for MLLE3[Rrm4] (665 – 791 AA; Fig. 1C, Fig. EV1A). Then, the rest of the C-terminal part

456   comprising amino acids 421 to 664 was resubmitted as input identifying other templates as a

457   new starting point for the MLLE2[Rrm4] (571-629). Likewise, the remaining C-terminal sequence

458   comprising amino acids 421 to 549 was resubmitted as input, identifying other templates as a

459   new starting point for the MLLE1[Rrm4] (446-530). In total, this led to the identification of three

460   MLLE domains, for which structural models were generated using default TopModel

461   parameters. The quality of the structural models was assessed with TopScore (Mulnaes &

462   Gohlke, 2018).

463   **Plasmids, strains, and growth conditions**

464   For molecular cloning of plasmids, *Escherichia coli* Top10 cells (Thermofisher C404010) and

465   for recombinant protein expression *E .coli Lobstr* cells (Kerafast EC1002) were used

466   respectively. Sequence encoding H-Rrm4-NT4 was inserted into the pET22 vector (Merck

467   69744) with an N-terminal hexa-histidine tag for crystallisation studies. Sequence encoding

468   MLLE variants were inserted into the pGEX-2T vector (Merck GE28-9546-53) containing GST

469   sequence in N-terminus for pulldown and ITC experiments. Sequence encoding PAM2 variants

470   were inserted into the Champion pET-Sumo vector (Thermofisher K30001). pRarepLys

471   plasmid was co-transformed in *E. coli Lobstr strain* to supplement the rare codons for efficient

472   recombinant protein production. *E. coli* transformation, cultivation, and plasmid isolation were

473   conducted using standard techniques. For yeast two-hybrid analyses *S. cerevisiae* strain AH109

474   (Matchmaker 3 system, Clontech) was used. Yeast cells were transformed and cultivated using

475   standard techniques. All *U. maydis* strains are derivatives of AB33, in which hyphal growth can

476   be induced by switching the nitrogen source in the medium (Brachmann *et al.*, 2001). *U. maydis*

477   yeast cells were incubated in complete medium (CM) supplemented with 1% glucose, whereas

478   hyphal growth was induced by changing to nitrate minimal medium (NM) supplemented with

479   1% glucose, both at 28°C (Brachmann *et al.*, 2001). Detailed growth conditions and general

480   cloning strategies for *U. maydis* are described elsewhere (Baumann *et al.*, 2012; Brachmann *et*

481   *al.*, 2004; Terfrüchte *et al.*, 2014). All plasmids were verified by sequencing. Strains were

482   generated by transforming progenitor strains with linearised plasmids. Successful integration

483   of constructs was verified by diagnostic PCR and by Southern blot analysis (Brachmann *et al.*,

484   2004). For ectopic integration, plasmids were linearised with *Ssp*I and targeted to the *ip*^{S} locus

485   (Loubradou *et al.*, 2001). A detailed description of all plasmids, strains, and oligonucleotides is

486   given in Appendix Tables S3–S9. Sequences are available upon request.

Recombinant protein expression and purification

488   *E. coli* cells from freshly transformed plates were inoculated in 20 ml expression media. In

489   order to produce high-density expression cultures with tight regulation of induction and

490   expression in shake flasks we designed a complex media inspired by the principle of Studier's

491   autoinduction media (Studier, 2005). We use adequate amount of glucose to prevent the

492   unintended induction and leaky expression of target protein as well as phosphate buffer to

493   prevent acidity as a result of glucose metabolism from the excessive glucose in the media. In

494   addition, the medium contained glycerol, nitrogen, sulphur, and magnesium for promoting

495   high-density growth. Unlike the Studier's autoinduction media our media lack lactose therefore

496   expression can be induced with IPTG and expressed at required temperature (Studier, 2005; 1.6

497   % Trypton, 1% Yeast extract, 50 mM Na_2HPO_4, 50 mM KH_2PO_4, 25 mM $[NH_4]_2SO_4$, 0.5%

498   Glycerol, 0.5% Glucose, 2 mM $MgSO_4$) with ampicillin (100 mg/ml) and chloramphenicol (34

499   mg/ml) or kanamycin (200 mg/ml) and chloramphenicol (34 mg/ml) and grown overnight (16

500   hours) at 37 °C, 200 rpm. Note that the high concentration of kanamycin was used to prevent

501   the unintended resistance promoted by high phosphate concentration (Studier, 2005).

502   Supernatant from the overnight culture was removed by centrifugation at 4 °C, 5000 × g for 2

503   minutes. Cells were resuspended in fresh media with a starting OD_{600} of 0.1 and grown at 37

504   °C, 200 rpm for about 2 hours 30 minutes until the OD_{600} = 1. Protein expression was induced

505   at 28 °C, 200 rpm, for 4 hours by addition of 1 mM IPTG, and harvested by centrifugation at

506   4°C, 6,000 × g for 5 minutes. Protein purification was performed as per the previous report

507   (Abts *et al.*, 2013). Hexa-histidine tagged protein was purified using Nickle-based affinity

508   chromatography (HisTrap HP, GE Healthcare) on Akta prime FPLC system. Cells were thawed

509   on ice and resuspended in buffer A (20 mM HEPES pH 8.0, 200 mM NaCl, 1 mM EDTA, 10

510   mM Imidazole pH 8.0; 1 mM PMSF, 0.5 mg/ml Lysozyme, 0.5 mg/ml DNase, 1mM β

511   mercaptoethanol [β-ME]). Subsequently, cells were lysed by sonication on ice and centrifuged

512   at 4 °C 18,000 × g for 30 minutes. Resulting supernatant was loaded on to a pre-equilibrated

513   column with buffer B (20 mM HEPES pH 8.0, 200 mM NaCl,10 mM Imidazole), washed with

514   buffer C (20 mM HEPES pH 8.0, 200 mM NaCl, 50 mM Imidazole, 1 mM β-ME), eluted with

515   buffer D (20 mM HEPES pH 8.0, 200 mM NaCl, 300 mM Imidazole, 1mM β-ME) and further

516   purified by Size Exclusion Chromatography (HiLoad 26/600 Superdex 200, GE Healthcare),

517   pre-equilibrated with buffer E (20 mM HEPES pH 8.0, 200 mM NaCl, 1 mM β-ME). For

518   crystallisation studies, H-Rrm4-NT4 was purified as above except that the buffers were

519   prepared with high salt (500 mM NaCl) and without β-ME.

520   GST-tagged protein was purified using Glutathione-based affinity chromatography (GSTrap

521   FF GE Healthcare). Cells were thawed on ice and resuspended in Buffer F (20 mM HEPES pH

522   8.0, 200 mM NaCl, 1 mM EDTA, pH 8.0; 1 mM PMSF, 0.1 mg/ml Lysozyme, 1 mM β-ME).

523   Subsequently, cells were lysed by sonication on ice and centrifuged at 4 °C, 18,000 g for 30

524   minutes. The resulting supernatant was loaded onto a pre-equilibrated column with buffer E (20

525   mM HEPES pH 8.0, 200 mM NaCl, 1 mM β-ME) and washed with the same buffer, eluted

526   with buffer H (20 mM HEPES pH 8.0, 200 mM NaCl, 10 mM reduced glutathione, 1 mM β-

527   ME), and further purified by size exclusion chromatography (HiLoad 16/600 Superdex 200 GE

528   Healthcare), pre-equilibrated with buffer E. Protein purity was analysed on SDS-PAGE. All the

529   purified proteins were concentrated, centrifuged at 4°C, $100,000 \times g$ for 30 minutes, quantified

530   by Nanodrop A280, aliquoted, and stored at -80°C. Peptides for ITC experiments were custom-

531   synthesised and purchased from Genscript, USA (see Fig. 3A for peptide sequence).

GST pull-down experiments

533   Pull-down assays were performed as per the previous report (Jankowski *et al.*, 2019). In short,

534   GST-MLLE variants and HS-PAM2 variants were expressed in *E. coli*. Cell pellets from 50 ml

535   *E. coli* expression culture were resuspended in 10 ml buffer F (20 mM HEPES pH 8.0, 200 mM

536   NaCl, 1 mM EDTA; 0.5% Nonidet P-40, 1 mM PMSF, 0.1 mg/ml Lysozyme). Cells were lysed

537   by sonication on ice and centrifuged at 4 °C, $16,000 \times g$ for 10 minutes. 1 mL of the resulting

538   supernatant was incubated for 1 hour at 4°C on constant agitation of 1,000 rpm with 100 μL

539   glutathione sepharose (GS) resin (GE Healthcare), pre-equilibrated in buffer F. The GS resin

540   was washed three times with 1 ml of buffer G (20 mM HEPES pH 8.0, 200 mM NaCl, 1 mM

541   EDTA, 0.5 % Nonidet P-40). Subsequently, supernatant of HS-PAM2 variants was added to

542   the GST-MLLE variant bound resins and incubated for 1 hour at 4 °C on agitation. The resins

543   were washed as aforementioned, resuspended in 100 μL of 2x Laemmli loading buffer, boiled

544   for 10 minutes at 95 °C and analysed by western blotting.

545 *Ustilago maydis* **cell disruption and sample preparation for immunoblotting**

546 *U. maydis* hyphae were induced as described earlier (see Plasmids, strains, and growth
547 conditions). 50 ml of hyphal cells (6 h.p.i) were harvested in a 50 ml conical centrifuge tubes
548 by centrifugation at $7,150 \times g$, for 5 minutes. Cell pellets were resuspended in 2 ml phosphate
549 buffered saline pH 7.0 (PBS; 137 mM NaCl, 2.7mM KCl, 8 mM Na_2HPO_4 and 2 mM KH_2PO_4)
550 and transferred to a 2 ml centrifuge tubes. Cells were harvested at $7,150 \times g$ for 5 minutes and
551 supernatant was removed completely. The resulting cell pellets were flash-frozen in liquid
552 nitrogen and stored at -80 °C until use. Sample tubes were placed on 24 well TissueLyser
553 adapter (Qiagen 69982) and soaked in liquid nitrogen for 1 minute, 5 mm stainless steel bead
554 was added to each sample tube and the cells were disrupted at 30 Hz for 3 times 1 minute in
555 Mixer Mill MM400 (Retsch, Germany), with intermittent cooling between shaking. At the end
556 of the cell disruption dry homogenised powder of cells were resuspended in 1 ml urea buffer (8
557 M urea, 50 mM Tris/HCl pH 8.0 containing one tablet of 'cOmplete' protease inhibitor per 25
558 ml, Roche, Germany; 1 mM DTT; 0.1 M PMSF) and centrifuged at $16,000 \times g$ for 10 minutes
559 at 4 °C. The supernatant was used for subsequent analysis. Samples were diluted ten times and
560 protein concentrations were measured by BCA assay (Thermofisher 23225). Samples were
561 diluted to 1 mg/ml final concentration in Laemmli buffer and boiled at 95 °C for 10 minutes.
562 40 µg of each sample was loaded in 1.5 mm thickness gels for SDS-PAGE, subsequently
563 analysed by Western blotting.

564 **Yeast two-hybrid analysis**

565 Yeast two-hybrid analyses were performed as per the previous report (Pohlmann *et al.*, 2015).
566 The two-hybrid system Matchmaker 3 from Clontech was used as per manufacturer's
567 instructions. Yeast strain AH109 was co-transformed with derivatives of pGBKT7-DS and
568 pGADT7-Sfi (Appendix Tables S8) and were grown on synthetic dropout plates (SD) without
569 leucine and tryptophan at 28 ˚C for 2 days. Transformants were patched on SD plates without
570 leucine and tryptophan (control) or on SD plates without leucine, tryptophan, histidine, and
571 adenine (selection). Plates were incubated at 28 ˚C for 2 days to test for growth under selection
572 condition. For qualitative plate assays, cells (SD -leu, -trp, OD600 of 0.5) were serially diluted
573 1:5 with sterile water, spotted 4 µl each on control and selection plates and incubated at 28 ˚C
574 for 2 days. Colony growth was documented with a LAS 4000 imaging system (GE Healthcare).

SDS-PAGE and immunoblotting

All SDS–PAGE and Western blotting experiments were performed as reported previously (Jankowski *et al.*, 2019). Western blotting samples were resolved by 8 or 10 or 12 % SDS-PAGE and transferred and immobilised on nitrocellulose membrane (Amersham Protran) by semi-dry blotting using Towbin buffer (25 mM Tris pH 8.6, 192 mM Glycine, 15% Methanol). Proteins were detected using α -His from mouse (Sigma H1029), α-Gfp from mouse, (Roche, Germany), α-tRfp from rabbit (AB233-EV, Evrogen) and α-Actin from mouse (MP Biomedicals, Germany) as primary antibodies. As secondary antibodies α-mouse IgG HRP conjugate (Promega W4021) or α-rabbit IgG HRP conjugate (Cell Signaling #7074) were used. Antibodies bound to nitrocellulose membranes were removed by incubating in TBS buffer pH 3.0 (50 Tris pH 3.0, 150mM NaCl) at room temperature, before detecting with the constitutively expressed control (α-Actin). Detection was carried out by using ECL^TM Prime (Cytiva RPN2236). Images were taken by luminescence image analyser, LAS4000 (GE Healthcare) as per the manufacturer's instructions.

Multiangle light scattering (MALS)

MALS was performed as per the previous report (Weiler *et al.*, 2021). Superdex 200 Increase 10/300 GL column (GE Healthcare) was pre-equilibrated overnight at 0.1 ml/minute flow ratewith buffer E (20 mM HEPES pH 8.0, 200 mM NaCl, 1 mM β-ME). For each analysis, 200 µl of a protein sample at 2.0 mg/ml concentration was loaded onto the column at 0.6 ml/minute flow rate using a 1260 binary pump (Agilent Technologies). The scattered light was measured with a miniDAWN TREOS II light scatterer, (Wyatt Technologies), and the refractive index was measured with an Optilab T-rEX refractometer, (Wyatt Technologies). Data analysis was performed with ASTRA 7.3.2.21 (Wyatt Technologies; Slotboom *et al.*, 2008).

Crystallisation of H-Rrm4 NT4

Initial crystallisation conditions were searched using MRC 3 96-well sitting drop plates and various commercially available crystallisation screens at 12 °C. 0.1 µl homogeneous protein solution (10 mg/ml in 20 mM Hepes pH 8.0, 500 mM NaCl) was mixed with 0.1 µl reservoir solution and equilibrated against 40 µl of the reservoir. After one week, initial rod-shaped crystals were found, which were then further optimised by slightly varying the precipitant concentrations. Optimisation was also performed in sitting drop plates (24-well) at 12 °C but by mixing 1 µl protein solution with 1 µl of the reservoir solution, equilibrated against 300 µl reservoir solution. Best diffracting crystals were grown within 7 days in 0.1 M Hepes pH 7.5,

607   20% (w/v) PEG 10000 (Qiagen PEG I, D5). Before harvesting the crystal, crystal-containing

608   drops were overlaid with 2 µl mineral oil and immediately flash-frozen in liquid nitrogen.

Data collection, processing, and structure refinement

610   A complete data set of the H-Rrm4-NT4 were collected at beamline ID23EH1 (ESRF, France)

611   at 100 K and wavelength 0.98 Å up to 2.6 Å resolution. All data were processed using the

612   automated pipeline at the EMBL HAMBURG and reprocessed afterwards using XDS (Kabsch,

613   2014). Above obtained model for MLLE2 by TopModel was successfully used to phase the 2.6

614   Å data set of Rrm4 MLLE using the program Phaser from the program suite Phenix (Afonine

615   *et al.*, 2012). The structure was then refined in iterative cycles of manual building and

616   refinement in coot (Emsley & Cowtan, 2004), followed by software-based refinements using

617   the program suite Phenix (Afonine *et al.*, 2012.) All residues were in the preferred and

618   additionally allowed regions of the Ramachandran plot (Appendix Table S2). The data

619   collection and refinement statistics are listed in Appendix Table S2. The structure and models

620   were combared using the superpose tool of PHENIX calculating the corresponding RMSD. The

621   images of the models were prepared using PyMOL. The structure was deposited at the

622   worldwide protein data bank under the accession code 7PZE.

Small angle X-ray scattering

624   We collected all SAXS data on beamline BM29 at the ESRF Grenoble (Pernot *et al.*, 2013;

625   Pernot *et al.*, 2010). The beamline was equipped with a PILATUS 2M detector (Dectris) with

626   a fixed sample to a distance of 2.827 m. To prevent concentration-dependent oligomerisation,

627   we performed the measurements with 0.6 mg/ml protein concentrations at 10 °C in buffer E.

628   We collected one frame each second and scaled the data to absolute intensity against water. All

629   used programs for data processing were part of the ATSAS Software package (Version

630   3.0.3;Manalastas-Cantos *et al.*, 2021). The primary data reduction was performed with the

631   program Primus (Konarev *et al.*, 2003). With Primus and the included Guinier approximation

632   (Franke & Svergun, 2009), we determined the forward scattering $I(0)$ and the radius of gyration

633   (R_g). The pair-distribution function $p(r)$ was calculated with Gnom (Svergun, 1992) and was

634   used to estimate the maximum particle dimension (D_{max}). Due to the high flexibility of the

635   proteins we performed an Ensemble Optimization Method (EOM; Tria *et al.*, 2015; default

636   parameters, 10,000 models in the initial ensemble, native-like models, constant subtraction

637   allowed) with the predicted MLLE domains from TopModel (Mulnaes *et al.*, 2021; Mulnaes *et*

638   *al.*, 2020b) for H-Rrm4-NT4 and G-Rrm4 with an additional GST (PDB1ua5). We uploaded

22

639   the data to the Small Angle Scattering Biological Data Bank (SASBDB; Kikhney *et al.*, 2020;

640   Valentini *et al.*, 2015) with the accession codes SASDMS5(G-Rrm4) and SASDMT5 (H-Rrm4-

641   NT4).

Isothermal titration calorimetry

643   All ITC experiments were performed as per the previous report (Abts *et al.*, 2013). All the

644   protein samples used in ITC were centrifuged at 451,000 × g for 30 minutes and quantified by

645   Nanodrop (A280) before use. The concentration of GST or His-tagged MLLE variants were

646   adjusted to 30 μM and PAM2 peptide variants were adjusted to 300 μM using buffer G (20 mM

647   HEPES pH 8.0, 200 mM NaCl, 1 mM 2 ME). Using an MicroCal iTC200 titration calorimeter

648   (Malvern Panalytical technologies), a PAM2 peptide variant with a volume of 40 μL was

649   titrated to the different GST-MLLE variants. All experiments were repeated at least twice. ITC

650   measurements were performed at 25 °C with 40 injections (1 μL each). Only the first injection

651   had a volume of 0.5 μL and was discarded from the isotherm. The other technical parameters

652   were reference power, 5 μcal s^{-1}; stirring speed, 1000 rpm; spacing time, 120 s, and a filter

653   period, 5 s. The resulting isotherm was fitted with a one-site binding model using MicroCal

654   Origin for ITC software (MicroCal LLC). Note, that the binding of GST-Rrm4-NT4 and H-

655   Rrm4-NT4 were comparable indicating that tagging of the Rrm4 versions did not influence the

656   binding affinity (Fig. 3B; Fig. EV3H).

Microscopy, image processing and image analysis

658   Laser-based epifluorescence-microscopy was performed on a Zeiss Axio Observer.Z1 as

659   previously described (Jankowski *et al.*, 2019). Co-localisation studies of dynamic processes

660   were carried out with a two-channel imager (DV2, Photometrics, Tucson, AZ, USA; Baumann

661   *et al.*, 2016). To quantify uni- and bipolar hyphal growth, cells were grown in 30 ml cultures to

662   an OD$_{600}$ of 0.5, and hyphal growth was induced. After 6 hours, more than 100 hyphae were

663   analysed per strains towards their growth behaviour (n = 3). Cells were assessed for unipolar

664   and bipolar growth as well as the formation of a basal septum. To analyse the signal number,

665   velocity, and travelled distance of fluorescently labelled proteins, movies with an exposure time

666   of 150 ms and 150 frames were recorded. More than 25 hyphae were analysed per strain (n =

667   3). To inhibit microtubule polymerisation, hyphal cultures were incubated with 50 μM of

668   benomyl (Sigma Aldrich) for 2 h at 28 °C and 200 rpm (Becht *et al.*, 2006). All movies and

669   images were processed and analysed using the Metamorph software (Version 7.7.0.0,

670   Molecular Devices, Seattle, IL, USA). For the generation of kymographs, 20 μm of hyphal cell

671 starting at the hyphal tip were used. To determine the minimum and maximum grey level
672 intensities of shuttling endosomes, 100 signals were analysed per strain (the ten most prominent
673 signals per kymograph that showed processive movement of > 20 μm without changes in
674 directions were chosen per strain). The minimum and maximum grey level intensities were
675 measured using the region measurement tool of the Metamorph software. All pixel intensities
676 were measured, minimum and maximum intensities for each region were listed (16 bit images).
677 The grey level intensities were normalised to the wild-type intensity, which was set to 100%.
678 For statistical analysis of the signal number, velocity, and travelled distance, processive signals
679 with a travelled distance of more than 5 μm were conducted and counted manually. For
680 determination of aberrant microtubule staining, hyphae were counted manually as well. Data
681 points represent means from three independent experiments ($n = 3$) with mean of means (red
682 line) and SEM. For all statistical evaluations, two-tailed Student´s t-tests were used.
683 Determination of strains exhibiting aberrant staining of microtubules were scored manually.
684 For verification, key comparisons were evaluated independently by two experimentalists.
685 Importantly, the key findings were confirmed (Fig. EV5H). We used the data obtained by the
686 more experienced microscopist in the main figure (Fig. 5D).

687

Acknowledgements

705

Author contributions

SKD, SSV, LS, SHJS, HG, and MF designed this study and analysed the data. SKD and SSV contributed equally to the structural biology of the MLLE binding platform; SKD performed the wet-lab experiments and SSV was responsible for modelling. KM and SKD performed the cell biological experiments. KM and LB coordinated strain generation and experimental design. JR, EH, AH contributed to SAXS, MALS, and X-ray analysis, respectively. SKD, SSV, LS, SHJS, HG, and MF drafted and revised the manuscript with input from all co-authors. SKD, SSV, SHJS, HG and MF directed the project.

714

Conflict of interest

The authors declare that they have no competing interests.

717

References

Abts A, Montalban-Lopez M, Kuipers OP, Smits SH, Schmitt L (2013) NisC binds the FxLx motif of the nisin leader peptide. *Biochemistry* 52: 5387-5395

Afonine PV, Grosse-Kunstleve RW, Echols N, Headd JJ, Moriarty NW, Mustyakimov M, Terwilliger TC, Urzhumtsev A, Zwart PH, Adams PD (2012) Towards automated crystallographic structure refinement with phenix.refine. *Acta Crystallogr D Biol Crystallogr* 68: 352-367

Albrecht M, Lengauer T (2004) Survey on the PABC recognition motif PAM2. *Biochem Biophys Res Commun* 316: 129-138

Baek M, DiMaio F, Anishchenko I, Dauparas J, Ovchinnikov S, Lee GR, Wang J, Cong Q, Kinch LN, Schaeffer RD *et al.* (2021) Accurate prediction of protein structures and interactions using a three-track neural network. *Science* 373: 871-876

Baumann S, König J, Koepke J, Feldbrügge M (2014) Endosomal transport of septin mRNA and protein indicates local translation on endosomes and is required for correct septin filamentation. *EMBO Rep* 15: 94-102

Baumann S, Pohlmann T, Jungbluth M, Brachmann A, Feldbrügge M (2012) Kinesin-3 and dynein mediate microtubule-dependent co-transport of mRNPs and endosomes. *J Cell Sci* 125: 2740-2752

736 Baumann S, Zander S, Weidtkamp-Peters S, Feldbrügge M (2016) Live cell imaging of septin
737   dynamics in *Ustilago maydis*. In: *Methods in Cell Biol: Septins*, Gladfelter A.S. (ed.) pp.
738   143-159. Elsevier Inc.:

739 Becht P, König J, Feldbrügge M (2006) The RNA-binding protein Rrm4 is essential for polarity
740   in *Ustilago maydis* and shuttles along microtubules. *J Cell Sci* 119: 4964-4973

741 Béthune J, Jansen RP, Feldbrügge M, Zarnack K (2019) Membrane-associated RNA-binding
742   proteins orchestrate organelle-coupled translation *Trends in cell biology* 29: 178-188

743 Brachmann A, König J, Julius C, Feldbrügge M (2004) A reverse genetic approach for
744   generating gene replacement mutants in *Ustilago maydis*. *Mol Gen Genom* 272: 216-226

745 Brachmann A, Weinzierl G, Kämper J, Kahmann R (2001) Identification of genes in the bW/bE
746   regulatory cascade in *Ustilago maydis*. *Mol Microbiol* 42: 1047-1063

747 Cioni JM, Lin JQ, Holtermann AV, Koppers M, Jakobs MAH, Azizi A, Turner-Bridger B,
748   Shigeoka T, Franze K, Harris WA *et al.* (2019) Late endosomes act as mRNA translation
749   platforms and sustain mitochondria in axons. *Cell* 176: 56-72 e15

750 Das S, Vera M, Gandin V, Singer RH, Tutucci E (2021) Intracellular mRNA transport and
751   localized translation. *Nat Rev Mol Cell Biol* 22: 483-504

752 Deo RC, Sonenberg N, Burley SK (2001) X-ray structure of the human hyperplastic discs
753   protein: an ortholog of the C-terminal domain of poly(A)-binding protein. *Proc Natl Acad*
754   *Sci U S A* 98: 4414-4419

755 Emsley P, Cowtan K (2004) Coot: model-building tools for molecular graphics. *Acta*
756   *Crystallogr D Biol Crystallogr* 60: 2126-2132

757 Fernandopulle MS, Lippincott-Schwartz J, Ward ME (2021) RNA transport and local
758   translation in neurodevelopmental and neurodegenerative disease. *Nature neuroscience*

759 Franke D, Petoukhov MV, Konarev PV, Panjkovich A, Tuukkanen A, Mertens HDT, Kikhney
760   AG, Hajizadeh NR, Franklin JM, Jeffries CM *et al.* (2017) ATSAS 2.8: a comprehensive
761   data analysis suite for small-angle scattering from macromolecular solutions. *J Appl*
762   *Crystallogr* 50: 1212-1225

763 Franke D, Svergun DI (2009) DAMMIF, a program for rapid ab-initio shape determination in
764   small-angle scattering. *J Appl Crystallogr* 42: 342-346

765 Grimm C, Pelz JP, Schneider C, Schaffler K, Fischer U (2020) Crystal structure of a variant
766   PAM2 motif of LARP4B bound to the MLLE domain of PABPC1. *Biomol* 10

767 Haag C, Steuten B, Feldbrügge M (2015) Membrane-coupled mRNA trafficking in fungi. *Annu*
768   *Rev Microbiol* 69: 265-281

769   Jankowski S, Pohlmann T, Baumann S, Müntjes KM, Devan SK, Zander S, Feldbrügge M
770   (2019) The multi PAM2 protein Upa2 functions as novel core component of endosomal
771   mRNA transport. *EMBO Rep* 24: e47381

772   Jinek M, Fabian MR, Coyle SM, Sonenberg N, Doudna JA (2010) Structural insights into the
773   human GW182-PABC interaction in microRNA-mediated deadenylation. *Nat Struct Mol*
774   *Biol* 17: 238-240

775   Jumper J, Evans R, Pritzel A, Green T, Figurnov M, Ronneberger O, Tunyasuvunakool K, Bates
776   R, Zidek A, Potapenko A *et al.* (2021) Highly accurate protein structure prediction with
777   AlphaFold. *Nature* 596: 583-589

778   Kabsch W (2014) Processing of X-ray snapshots from crystals in random orientations. *Acta*
779   *Crystallogr D Biol Crystallogr* 70: 2204-2216

780   Kikhney AG, Borges CR, Molodenskiy DS, Jeffries CM, Svergun DI (2020) SASBDB:
781   Towards an automatically curated and validated repository for biological scattering data.
782   *Protein Sci* 29: 66-75

783   Konarev PV, Volkov VV, Sokolova AV, Koch MHJ, Svergun DI (2003) PRIMUS: a Windows
784   PC-based system for small-angle scattering data analysis. *J Appl Crystallogr* 36: 1277-
785   1282

786   Kozlov G, De Crescenzo G, Lim NS, Siddiqui N, Fantus D, Kahvejian A, Trempe JF, Elias D,
787   Ekiel I, Sonenberg N *et al.* (2004) Structural basis of ligand recognition by PABC, a highly
788   specific peptide-binding domain found in poly(A)-binding protein and a HECT ubiquitin
789   ligase. *EMBO J* 23: 272-281

790   Kozlov G, Gehring K (2010) Molecular basis of eRF3 recognition by the MLLE domain of
791   poly(A)-binding protein. *PLoS One* 5: e10169

792   Kozlov G, Menade M, Rosenauer A, Nguyen L, Gehring K (2010) Molecular determinants of
793   PAM2 recognition by the MLLE domain of poly(A)-binding protein. *J Mol Biol* 397: 397-
794   407

795   Kozlov G, Trempe JF, Khaleghpour K, Kahvejian A, Ekiel I, Gehring K (2001) Structure and
796   function of the C-terminal PABC domain of human poly(A)-binding protein. *Proc Natl*
797   *Acad Sci U S A* 98: 4409-4413

798   Liao YC, Fernandopulle MS, Wang G, Choi H, Hao L, Drerup CM, Patel R, Qamar S, Nixon-
799   Abell J, Shen Y *et al.* (2019) RNA granules hitchhike on lysosomes for long-distance
800   transport, using annexin A11 as a molecular tether. *Cell* 179: 147-164 e120

801   Lim NS, Kozlov G, Chang TC, Groover O, Siddiqui N, Volpon L, De Crescenzo G, Shyu AB,
802   Gehring K (2006) Comparative peptide binding studies of the PABC domains from the

803   ubiquitin-protein isopeptide ligase HYD and poly(A)-binding protein. Implications for

804   HYD function. *The Journal of biological chemistry* 281: 14376-14382

805 Loubradou G, Brachmann A, Feldbrügge M, Kahmann R (2001) A homologue of the

806   transcriptional repressor Ssn6p antagonizes cAMP signalling in *Ustilago maydis. Mol*

807   *Microbiol* 40: 719-730

808 Manalastas-Cantos K, Konarev PV, Hajizadeh NR, Kikhney AG, Petoukhov MV, Molodenskiy

809   DS, Panjkovich A, Mertens HDT, Gruzinov A, Borges C *et al.* (2021) ATSAS 3.0:

810   expanded functionality and new tools for small-angle scattering data analysis. *J Appl*

811   *Crystallogr* 54

812 Mangus DA, Amrani N, Jacobson A (1998) Pbp1p, a factor interacting with *Saccharomyces*

813   *cerevisiae* poly(A)-binding protein, regulates polyadenylation. *Molecular and cellular*

814   *biology* 18: 7383-7396

815 Mangus DA, Evans MC, Jacobson A (2003) Poly(A)-binding proteins: multifunctional

816   scaffolds for the post-transcriptional control of gene expression. *Genome Biol* 4: 223

817 Mattijssen S, Kozlov G, Fonseca BD, Gehring K, Maraia RJ (2021) LARP1 and LARP4: up

818   close with PABP for mRNA 3' poly(A) protection and stabilization. *RNA Biol* 18: 259-274

819 Mofatteh M, Bullock SL (2017) SnapShot: Subcellular mRNA localization. *Cell* 169: 178.e171

820 Müller J, Pohlmann T, Feldbrügge M (2019) Core components of endosomal mRNA transport

821   are evolutionarily conserved in fungi. *Fungal Genet Biol* 126: 12-16

822 Mulnaes D, Gohlke H (2018) TopScore: using deep neural networks and large diverse data sets

823   for accurate protein model quality assessment. *J Chem Theory Comput* 14: 6117-6126

824 Mulnaes D, Koenig F, Gohlke H (2021) TopSuite Web Server: A Meta-Suite for Deep-

825   Learning-Based Protein Structure and Quality Prediction. *Journal of chemical information*

826   *and modeling* 61: 548-553

827 Mulnaes D, Porta N, Clemens R, Apanasenko I, Reiners J, Gremer L, Neudecker P, Smits SHJ,

828   Gohlke H (2020a) TopModel: template-based protein structure prediction at low sequence

829   identity using top-down consensus and deep neural networks. *J Chem Theory Comput* 16:

830   1953-1967

831 Mulnaes D, Porta N, Clemens R, Apanasenko I, Reiners J, Gremer L, Neudecker P, Smits SHJ,

832   Gohlke H (2020b) TopModel: Template-Based Protein Structure Prediction at Low

833   Sequence Identity Using Top-Down Consensus and Deep Neural Networks. *J Chem*

834   *Theory Comput* 16: 1953-1967

835   Munoz-Escobar J, Matta-Camacho E, Kozlov G, Gehring K (2015) The MLLE domain of the
836   ubiquitin ligase UBR5 binds to its catalytic domain to regulate substrate binding. *The*
837   *Journal of biological chemistry* 290: 22841-22850

838   Müntjes K, Devan SK, Reichert AS, Feldbrügge M (2021) Linking transport and translation of
839   mRNAs with endosomes and mitochondria. *EMBO reports* accepted for publication

840   Müntjes K, Philipp M, Husemann L, Heucken N, Weidtkamp-Peters S, Schipper K, Zurbriggen
841   MD, Feldbrügge M (2020) Establishing polycistronic expression in the model
842   microorganism *Ustilago maydis*. *Front Microbiol* 11: 1384

843   Niessing D, Jansen RP, Pohlmann T, Feldbrügge M (2018) mRNA transport in fungal top
844   models. *Wiley interdisciplinary reviews RNA* 9: e1453

845   Olgeiser L, Haag C, Boerner S, Ule J, Busch A, Koepke J, König J, Feldbrügge M, Zarnack K
846   (2019) The key protein of endosomal mRNP transport Rrm4 binds translational landmark
847   sites of cargo mRNAs. *EMBO Rep* 20: e46588

848   Pernot P, Round A, Barrett R, De Maria Antolinos A, Gobbo A, Gordon E, Huet J, Kieffer J,
849   Lentini M, Mattenet M *et al.* (2013) Upgraded ESRF BM29 beamline for SAXS on
850   macromolecules in solution. *Journal of synchrotron radiation* 20: 660-664

851   Pernot P, Theveneau P, Giraud T, Fernandes RN, Nurizzo D, Spruce D, Surr J, McSweeney S,
852   Round A, Felisaz F *et al.* (2010) New beamline dedicated to solution scattering from
853   biological macromolecules at the ESRF. *Journal of Physics: Conference Series* 247:
854   012009

855   Pohlmann T, Baumann S, Haag C, Albrecht M, Feldbrügge M (2015) A FYVE zinc finger
856   domain protein specifically links mRNA transport to endosome trafficking. *eLife* 4: e06041

857   Quentin D, Schuhmacher JS, Klink BU, Lauer J, Shaikh TR, Huis in t´t Veld PJ, Welp LM,
858   Urlaub H, Zerial M, Raunser S (2021) Structure of the human FERRY Rab5 effector
859   complex. *bioRiv* 10.1101/2021.06.21.449265

860   Sawazaki R, Imai S, Yokogawa M, Hosoda N, Hoshino SI, Mio M, Mio K, Shimada I, Osawa
861   M (2018) Characterization of the multimeric structure of poly(A)-binding protein on a
862   poly(A) tail. *Sci Rep* 8: 1455

863   Schäfer IB, Yamashita M, Schuller JM, Schussler S, Reichelt P, Strauss M, Conti E (2019)
864   Molecular bsis for poly(A) RNP architecture and recognition by the Pan2-Pan3
865   deadenylase. *Cell* 177: 1619-1631 e1621

866   Schuhmacher JS, Dieck ST, Christoforidis S, Landerer C, Hersemann L, Seifert S, Giner A,
867   Toth-Petroczy A, Kalaidzidis Y, Schumann EM *et al.* (2021) The novel Rab5 effector

868   FERRY links early endosomes with the translation machinery. *BioRiv*
869   10.1101/2021.06.20.449167

870 Slotboom DJ, Duurkens RH, Olieman K, Erkens GB (2008) Static light scattering to
871   characterize membrane proteins in detergent solution. *Methods* 46: 73-82

872 Stenmark H, Aasland R, Driscoll PC (2002) The phosphatidylinositol 3-phosphate-binding
873   FYVE finger. *FEBS Lett* 513: 77-84

874 Studier FW (2005) Protein production by auto-induction in high density shaking cultures.
875   *Protein Expr Purif* 41: 207-234

876 Su H, Meng S, Lu Y, Trombly MI, Chen J, Lin C, Turk A, Wang X (2011) Mammalian
877   hyperplastic discs homolog EDD regulates miRNA-mediated gene silencing. *Mol Cell* 43:
878   97-109

879 Svergun DI (1992) Determination of the regularization parameter in indirect-transform methods
880   using perceptual criteria. . *J Appl Crystallogr* 25: 495-503

881 Terfrüchte M, Joehnk B, Fajardo-Somera R, Braus G, Riquelme M, Schipper K, Feldbrügge M
882   (2014) Establishing a versatile Golden Gate cloning system for genetic engineering in
883   fungi. *Fungal Genet Biol* 62: 1-10

884 Tian L, Chou HL, Fukuda M, Kumamaru T, Okita TW (2020a) mRNA localization in plant
885   cells. *Plant Physiol* 182: 97-109

886 Tian L, Chou HL, Zhang L, Hwang SK, Starkenburg SR, Doroshenk KA, Kumamaru T, Okita
887   TW (2018) RNA-binding protein RBP-P is required for glutelin and prolamine mRNA
888   localization in rice endosperm cells. *Plant Cell* 30: 2529-2552

889 Tian L, Doroshenk KA, Zhang L, Fukuda M, Washida H, Kumamaru T, Okita T (2020b)
890   Zipcode RNA-binding proteins and membrane trafficking proteins cooperate to transport
891   glutelin mRNAs in rice endosperm. *Plant Cell* 32: 2566-2581

892 Tria G, Mertens HD, Kachala M, Svergun DI (2015) Advanced ensemble modelling of flexible
893   macromolecules using X-ray solution scattering. *IUCrJ* 2: 207-217

894 Valentini E, Kikhney AG, Previtali G, Jeffries CM, Svergun DI (2015) SASBDB, a repository
895   for biological small-angle scattering data. *Nucleic Acids Res* 43: D357-363

896 Weiler AJ, Spitz O, Gudzuhn M, Schott-Verdugo SN, Kamel M, Thiele B, Streit RW, Kedrov
897   A, L. S, Gohlke H *et al.* (2021) Novel intracellular phospholipase B from *Pseudomonas*
898   *aeruginosa* with activity towards endogenous phospholipids affects biofilm assembly.
899   *bioRiv* doi.org/10.1101/2021.06.15.448513

900 Xie J, Kozlov G, Gehring K (2014) The "tale" of poly(A) binding protein: the MLLE domain
901   and PAM2-containing proteins. *Biochim Biophys Acta* 1839: 1062-1068

902   Yang R, Gaidamakov SA, Xie J, Lee J, Martino L, Kozlov G, Crawford AK, Russo AN, Conte
903   MR, Gehring K *et al.* (2011) La-related protein 4 binds poly(A), interacts with the poly(A)-
904   binding protein MLLE domain via a variant PAM2w motif, and can promote mRNA
905   stability. *Mol Cell Biol* 31: 542-556
906   Zander S, Baumann S, Weidtkamp-Peters S, Feldbrügge M (2016) Endosomal assembly and
907   transport of heteromeric septin complexes promote septin cytoskeleton formation. *J Cell*
908   *Sci* 129: 2778-2792

Devan, Schott-Verdugo *et al.*

909 **Figures**

910
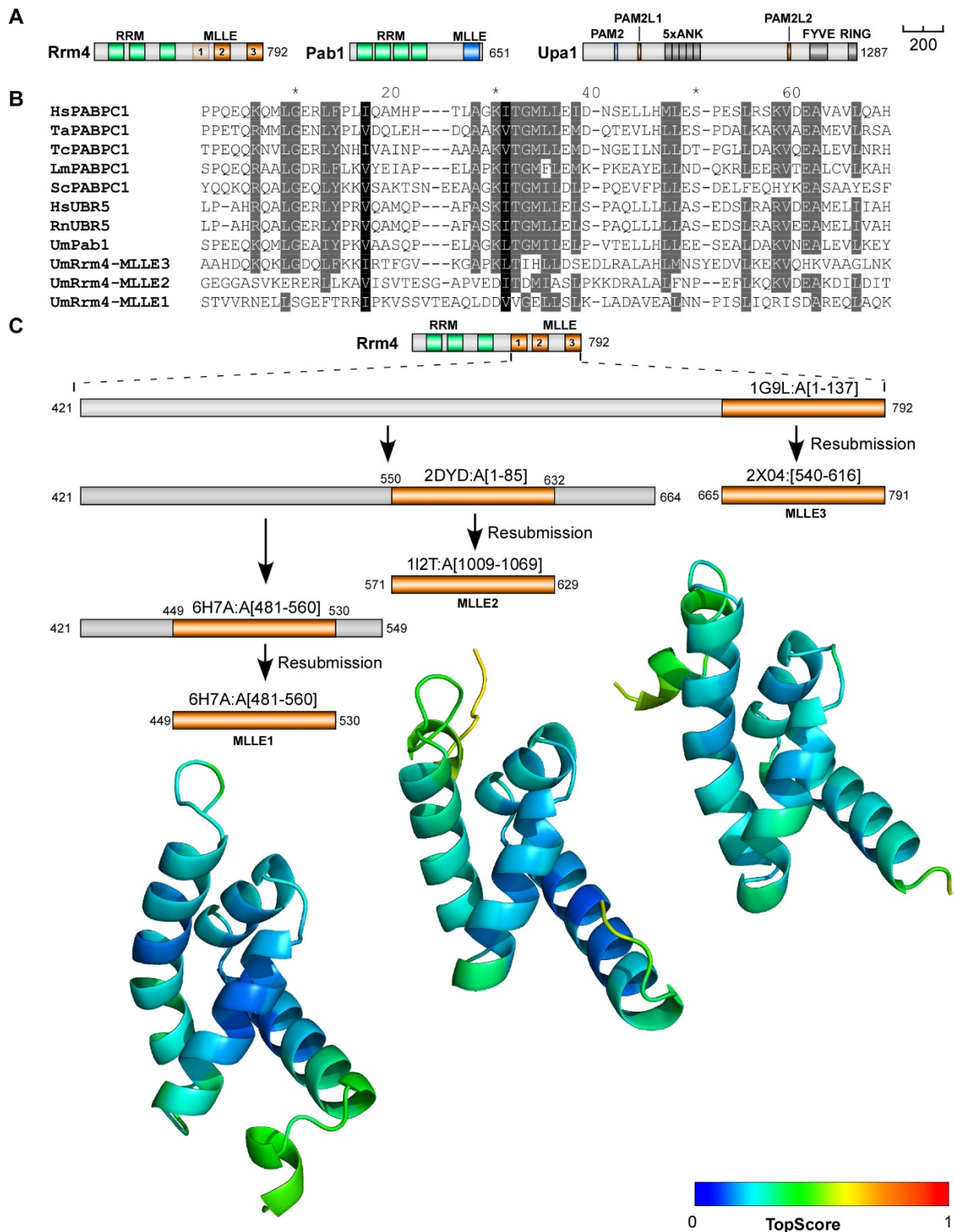
Figure 1. The C-terminal half of Rrm4 contains three MLLE domains.

912 (**A**) Schematic representation of protein variants drawn to scale (bar, 200 amino acids, number
913 of amino acids indicated next to protein bars) using the following colouring: dark green, RNA

32

914 recognition motif (RRM); orange, MLLE^{Rrm4} domains; dark blue, MLLE^{Pab1}; light blue PAM2;

915 light orange PAM2L sequence (PL1 – 2) Ankyrin repeats (5xANK), FYVE domain, and RING

916 domain of Upa1 are given in dark grey. (**B**) Sequence alignment of previously determined

917 MLLE domains showing the degree of similarity to the three Rrm4-MLLE domains and the

918 positions (Hs - *Homo sapiens*, Ta - *Triticum aestivum*, La - *Leishmania major*, Sc -

919 *Saccharomyces cerevisiae*, Tc - *Trypanosoma cruzi*, Rn - *Rattus norvegicus*, Um - *Ustilago*

920 *maydis*, PABPC1, Pab1 – poly [A]-binding protein, UBR5 - E3 ubiquitin-protein ligase).

921 Accession number and sequence coverage are listed in the Appendix Table S1. Multiple

922 sequence alignment was performed by ClustalW. (**C**) Identification and modelling of C-

923 terminal MLLE domains of Rrm4. The iterative process is depicted graphically. The best-

924 identified template for each run, and the region of that template that aligns with Rrm4, are

925 displayed (see also Fig. EV1A for the templates used for the final models). The structural

926 models obtained are shown for the span of the first identified template and are coloured

927 according to their per-residue TopScore, where the scale from 0 to 1 indicates a low to high

928 local structural error.

929
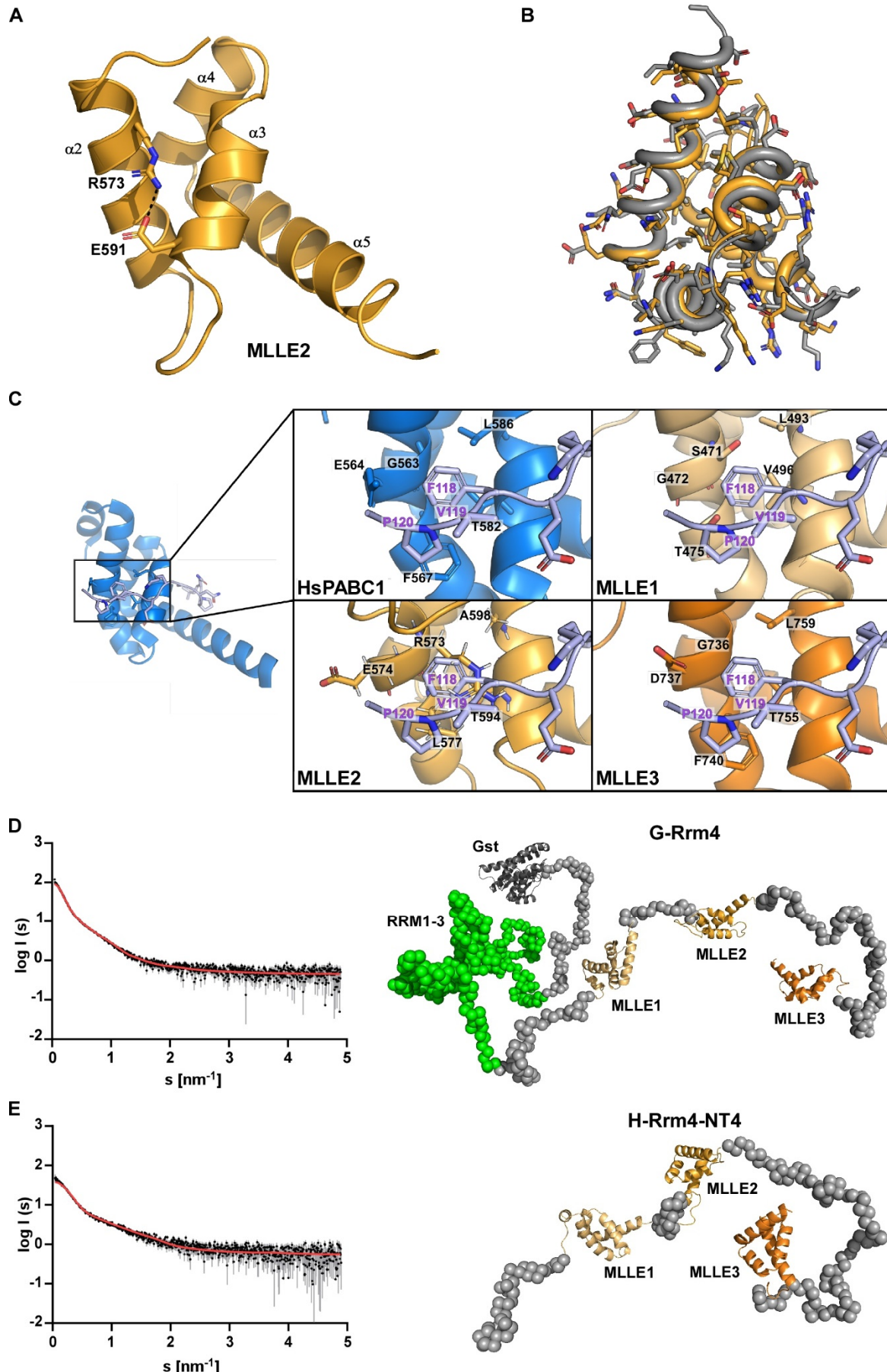
Figure 2. Rrm4 contains a C-terminal tripartite MLLE binding platform

932   (**A**) Crystal structure of the MLLE2 domain is highlighted in orange. The four helices are
933   indicated by α2-5 according to the 5 helix nomenclature found in MLLE domains (Xie *et al.*,
934   2014). Note that the first short helix α1 is missing. Arg573 and Glu591 are highlighted in the
935   sticks. These sides chains would interfere with the binding of the canonical Phe of PAM2 type
936   motifs. (**B**) Structural alignment of the MLLE2 model generated by TopModel and the X-ray
937   crystal structure of this domain (grey or orange, respectively). The all-atom RMSD is 0.69 Å,
938   resulting mostly from different rotamers of solvent-exposed sidechains. (**C**) Comparison of
939   peptide-binding sites after structural alignment of the models of Rrm4 MLLE domains (orange
940   shades) and the canonical MLLE domain of HsPABPC1 (blue; PDB ID 3KUS) and manually
941   placing the PAM2 motif of PAIP2 (lilac). In the interaction of MLLE^{PABPC1} with PAM2 of
942   PAIP2, Phe118 of PAM2 is the major determinant for binding and present in all the PAM2
943   motifs except LARP4a and b (Kozlov & Gehring, 2010; Xie *et al.*, 2014; Fig. EV3A). Of the
944   identified Rrm4 MLLE domains, only MLLE3 retains all sidechains that favour the binding of
945   this characteristic Phe; particularly, Gly736 should allow the Phe to bind into a pocket. MLLE1
946   and MLLE2 have Ser471 and Arg573 instead of G in this position, suggesting that Phe binding
947   would be sterically hindered in these interfaces. (**D**) *Left panel* Experimental data curve for
948   GST-Rrm4 is shown in black dots with grey error bars, the EOM fit as a red line (χ^2 =1.289).
949   The intensity is displayed as a function of momentum transfers. *Right panel* Selected model of
950   the EOM analysis from GST-Rrm4 with a R_g of 8.75 nm, a D_{max} of 23.99 nm with a volume
951   fraction of~0.25. (**E**) *left panel* Experimental data curve for H-Rrm4NT4 is shown in black dots
952   with grey error bars, the EOM fit as the red line (χ^2 =1.262). The intensity is displayed as a
953   function of momentum transfers. *right panel* Selected model of the EOM analysis from H-
954   Rrm4NT4 with a R_g of 5.10 nm, a D_{max} of 16.43 nm, and a volume fraction of~0.75. The MLLE
955   subdomains are shown in cartoon representation (MLLE1 in light orange, MLLE2 in orange,
956   MLLE 3 in dark orange, and the GST in dark grey) and the missing amino acids as grey spheres
957   (all other models and the SAXS data are available in Fig. EV2E).
958
959
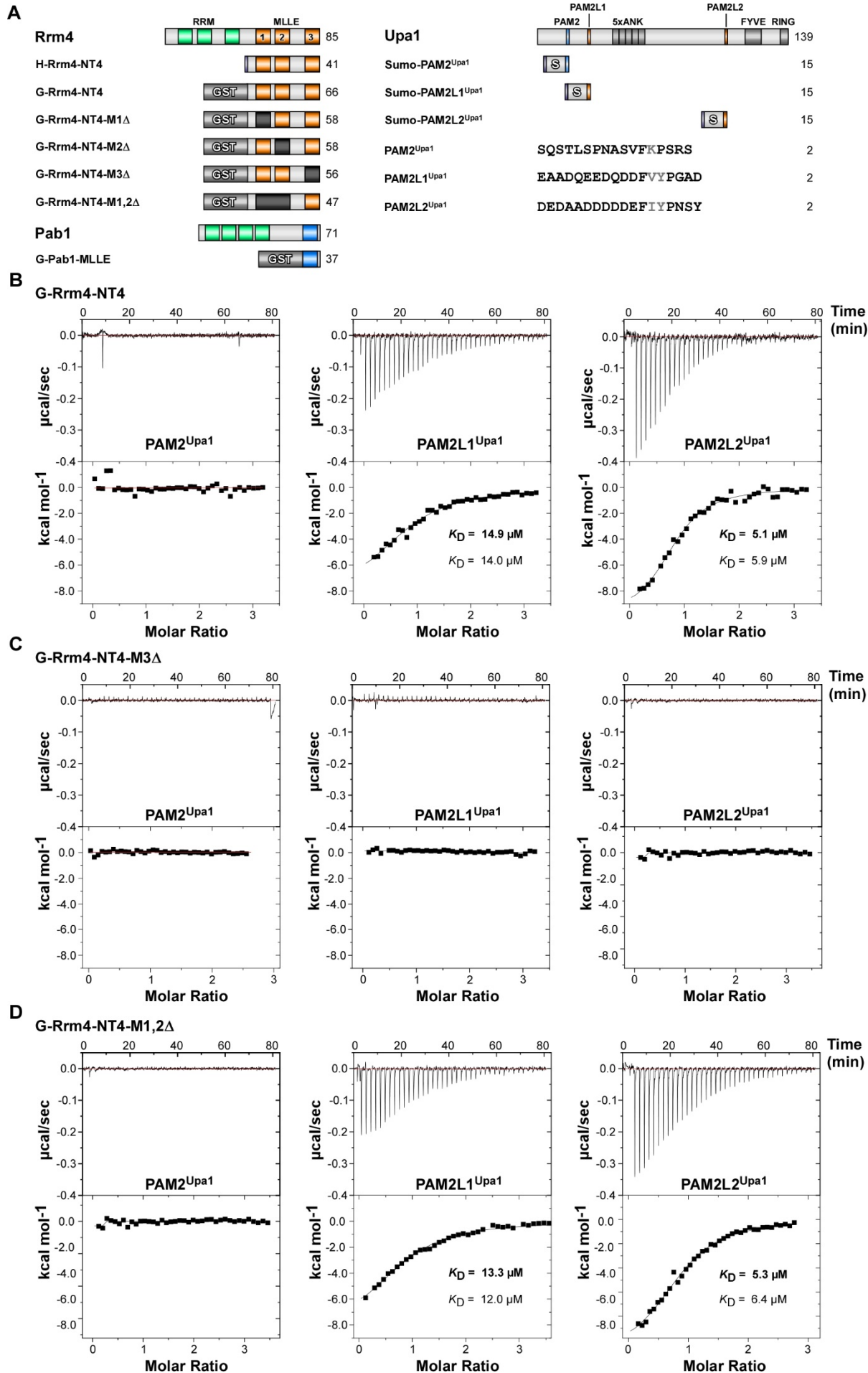
961 **Figure 3. MLLE3^{Rrm4} is crucial for PAM2L1^{Upa1} and PAM2L2^{Upa1} binding.**

962 (**A**) Schematic representation of protein variants (Molecular weight in kilo Dalton indicated)
963 using the following colouring: dark green, RNA recognition motif (RRM); orange, MLLE^{Rrm4}
964 domains; dark blue, MLLE^{Pab1}; light blue PAM2; light orange PAM2L sequence (PL1 – 2).
965 Ankyrin repeats (5xANK), FYVE domain, and RING domain of Upa1 are given in dark grey.
966 GST and SUMO tags are labelled. Variant amino acids of the FxP and FxxP of PAM2 and
967 PAM2L sequences are printed in grey font. (**B-D**) Representative isothermal titration
968 calorimetry (ITC) binding curves of MLLE domains. Experiments were performed using GST-
969 or Histidine-tagged MLLE variants and synthetic PAM2 peptide variants. K_D values of two
970 independent measurements are given (values corresponding to the indicated data are given in
971 bold).

Devan, Schott-Verdugo *et al.*

972
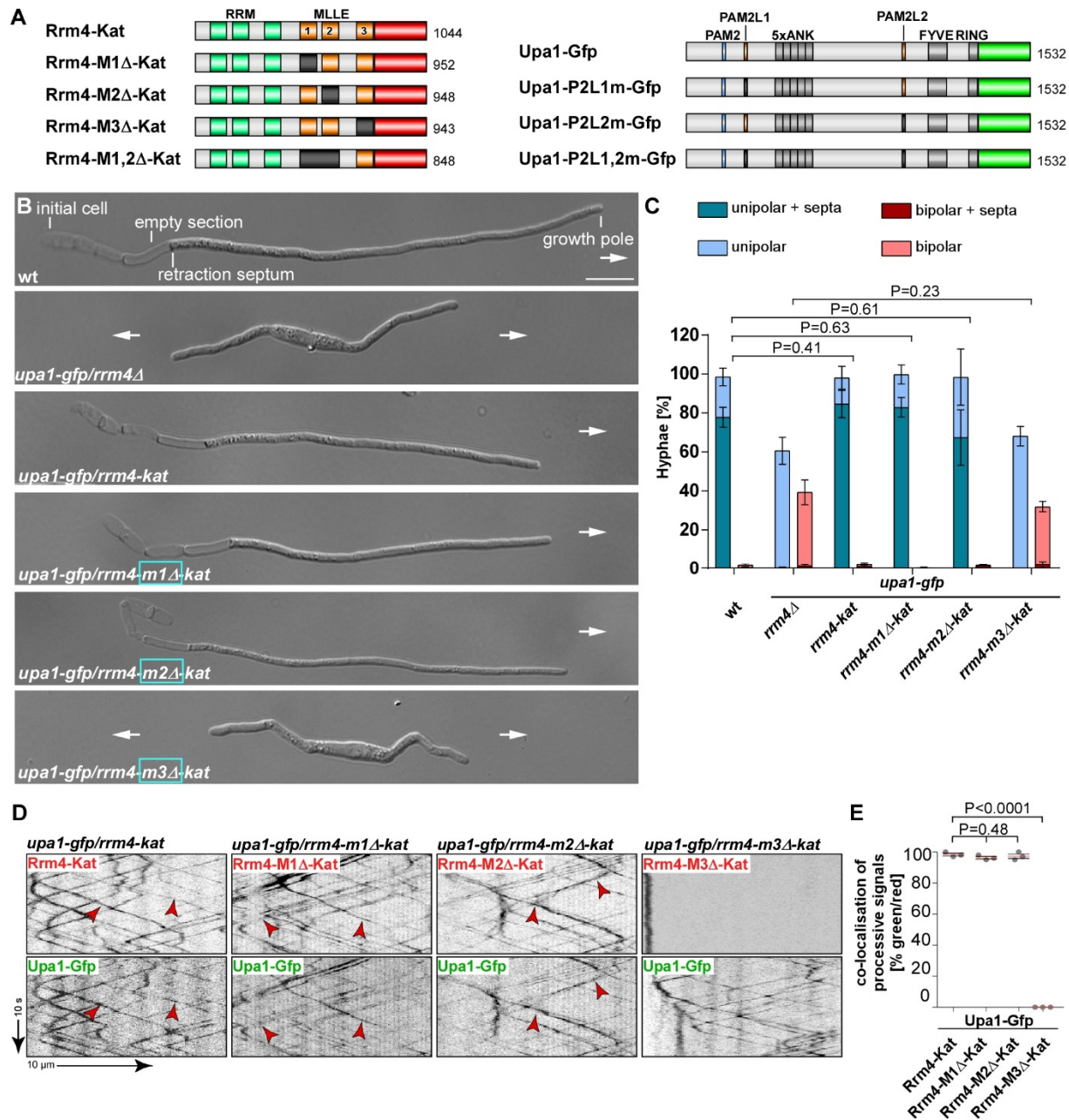
Figure 4. MLLE3 is key for endosomal mRNA transport.

(**A**) Schematic representation of Rrm4 and Upa1 variants drawn not to scale (number of amino acids indicated next to protein bars) using the following colouring: dark green, RNA recognition motif (RRM); orange, MLLE domains; red, mKate2, blue, PAM2, light orange PAM2 like sequence (PL1 – 2) and light green, Gfp. Ankyrin repeats (5xANK), FYVE domain and RING domain of Upa1 are given in dark grey. (**B**) Growth of AB33 derivatives in their hyphal form (6 h.p.i.; size bar 10 μm). Growth direction is marked by arrows. (**C**) Quantification of hyphal growth of AB33 derivatives shown in B (6 h.p.i.): unipolarity, bipolarity and basal septum formation were quantified (error bars, SEM.; n = 3 independent experiments, > 100 hyphae were counted per strain; for statistical evaluation, the percentage of uni- and bipolarity was investigated by using unpaired two-tailed Student's t-test ($\alpha < 0.05$). (**D**) Kymographs of AB33 hyphae derivatives (6 h.p.i.; inverted fluorescence images) expressing pairs of red and green

38

985   fluorescent proteins as indicated. Fluorescence signals were detected simultaneously using
986   dual-view technology (arrow length on the left and bottom indicates time and distance,
987   respectively). Processive co-localising signals are marked by red arrowheads. (**E**) Percentage
988   of processive signals exhibiting co-localisation for strains shown in D (data points represent
989   means from n = 3 independent experiments, with mean of means, red line and SEM; unpaired
990   two-tailed Student's t-test ($\alpha < 0.05$); for each experiment, 10 hyphae per strains were analysed).
991

992
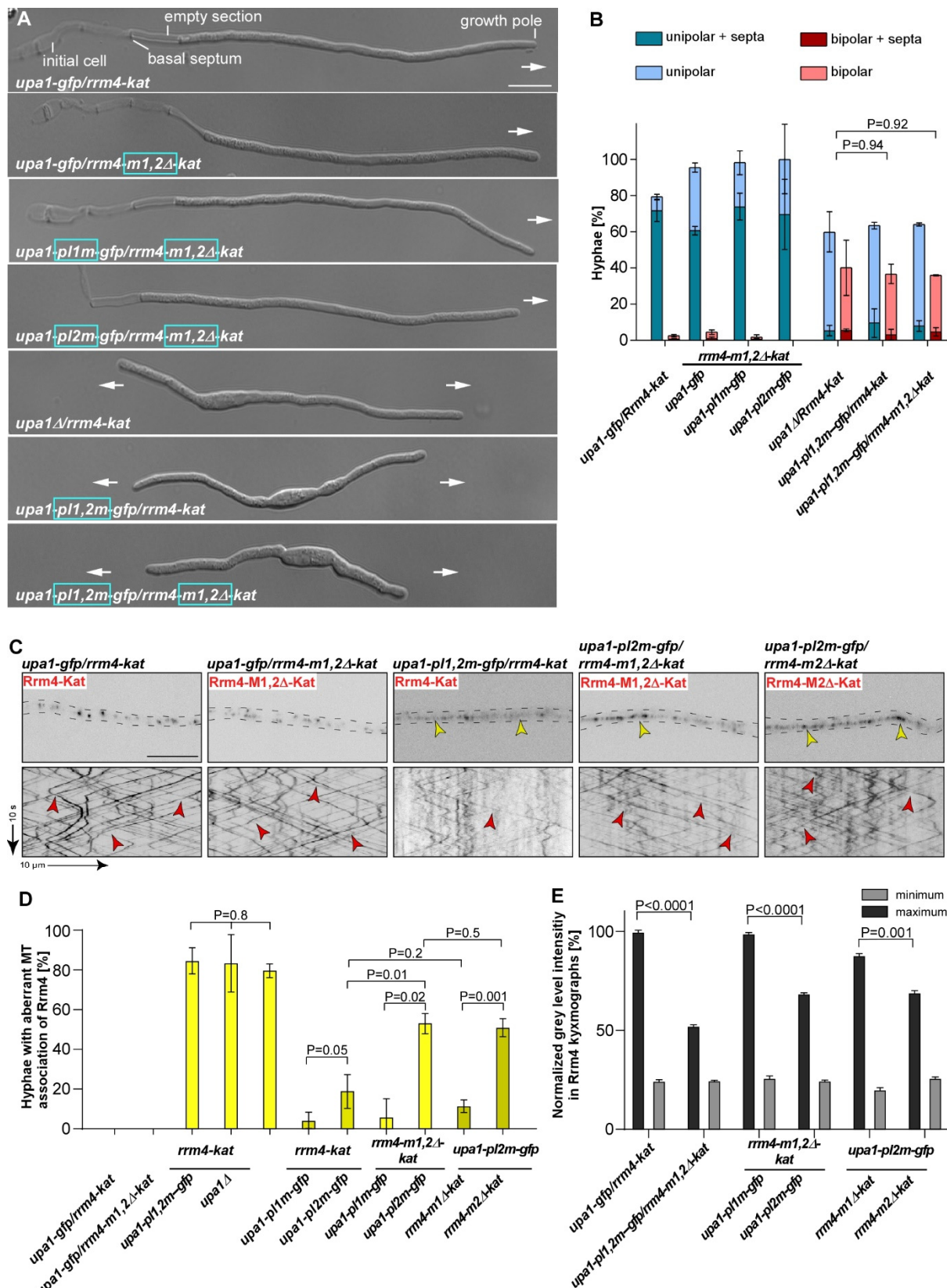
Figure 5. MLLE2 plays an accessory role in endosomal attachment of Rrm4

(**A**) Growth of AB33 derivatives in their hyphal form (6 h.p.i.; size bar 10 μm). Growth direction is marked by arrows. (**B**). Quantification of hyphal growth of AB33 derivatives shown in A (6 h.p.i.): unipolarity, bipolarity and basal septum formation were quantified (error bars,

40

997   SEM; n = 3 independent experiments, > 100 hyphae were analysed per strain; For statistical
998   analysis, the percentage of uni- and bipolarity was investigated by using unpaired two-tailed
999   Student's t-test (α<0.05). (**C**) Micrographs (inverted fluorescence image; size bar, 10 µm) and
1000   corresponding kymographs of AB33 hyphae derivatives (6 h.p.i.) co-expressing various Upa1-
1001   Gfp and Rrm4-Kat versions as indicated. Movement of Rrm4-Kat versions is shown (arrow
1002   length on the left and bottom indicates time and distance, respectively). Bidirectional movement
1003   is visible as diagonal lines (red arrowheads). Aberrant microtubule staining is indicated by a
1004   yellow arrowhead. (**D**) Percentage of hyphae (6 h.p.i.) exhibiting aberrant microtubule
1005   association as indicated in panel C and EV5C. Set of strains that were analysed simultaneously
1006   are shown in the same yellow shading (error bars, SEM; for statistical evaluation, the percentage
1007   of hyphae with abnormal microtubule staining was compared by using unpaired two-tailed
1008   Student's t-test (α<0.05); n = 3 independent experiments, > 25 hyphae were analysed per
1009   strain). (**E**) Normalised minimum and maximum grey level intensities of shuttling signals
1010   measured in Rrm4 kymographs showed in Fig. 5C and Fig. EV5C (error bars, SEM; n = 3
1011   independent experiments, 100 shuttling signals kymographs were analysed per strain, two-
1012   tailed Student's t-test (α > 0.05).
1013
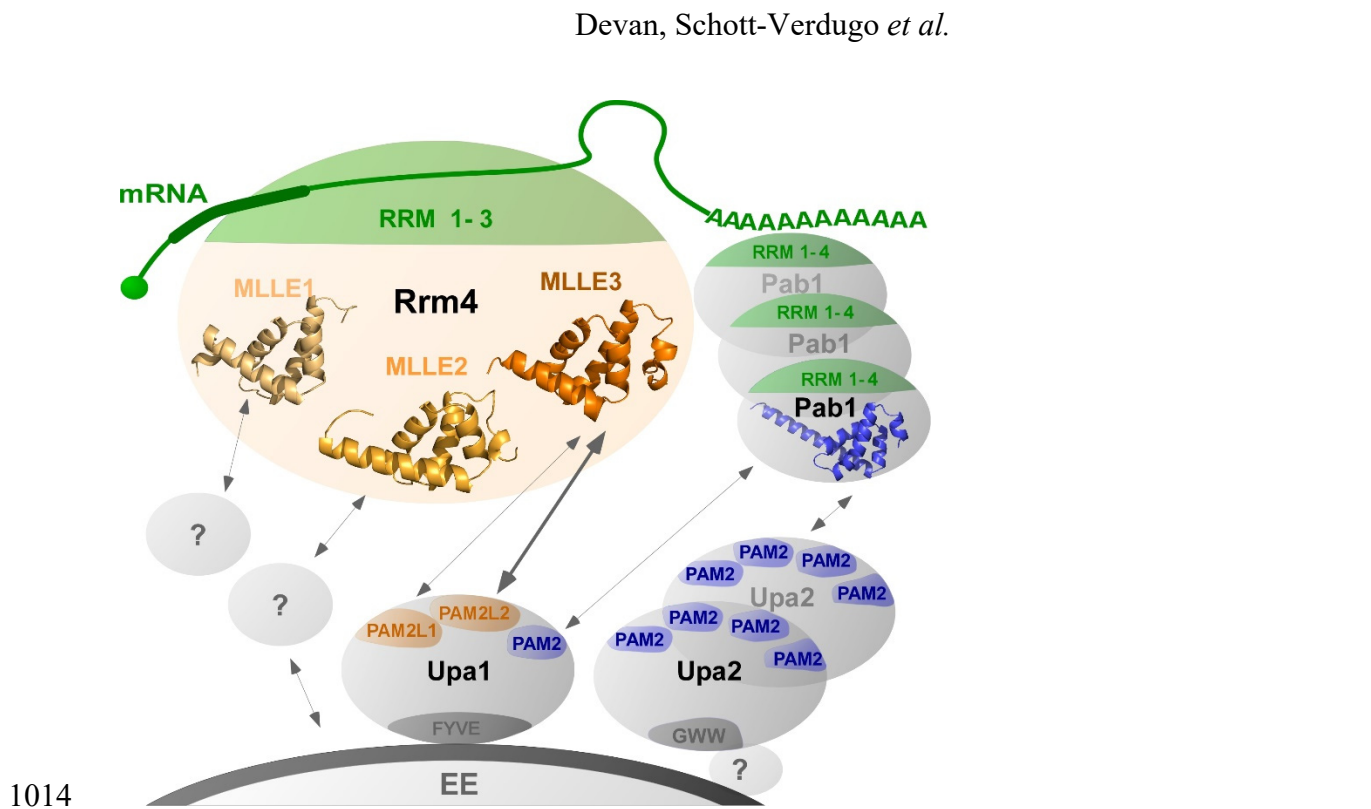
Figure 6. Schematic model of endosomal attachment of mRNPs via MLLE domains

Cargo mRNAs (green) are bound by the N-terminal RRM (1-3) domains of Rrm4 (green). The C terminal MLLE domains (orange) form a binding platform: MLLE3^{Rrm4} interacts with PAM2L1^{Upa1} and PAM2L2^{Upa1}(orange), MLLE1 and -2^{Rrm4} might interact with currently unknown factors to support the endosomal binding. In particular, MLLE2^{Rrm4} has an accessory role during endosomal interaction. The four RRMs of Pab1 (green) interact with the poly(A) tail, and the MLLE^{Pab1} (blue) interacts with PAM2 of Upa1 and with the four PAM2 motifs of Upa2 (dark blue), a dimerising scaffold protein. Upa1 is attached to endosomes via its FYVE domain, and the C-terminal GWW motif of Upa2 is crucial for its endosomal binding.

Devan, Schott-Verdugo *et al.*

1025

Expanded View Figures

A

Domain	Templates[a]	Rrm4 span	Template span	Identity (Similarity)[b]
MLLE1	6H7A:A	451-529	481-560	22.1 (38.4)
	3PTH:A	451-528	544-618	18.4 (34.5)
	1I2T:A	464-528	1009-1069	25.8 (40.9)
MLLE2	1I2T:A	571-629	1009-1069	23.8 (44.4)
	3KTP:A	550-631	554-620	17.6 (35.3)
	3KUR:A	550-627	554-616	18.5 (37.0)
MLLE3	2X04:A	712-791	540-616	30.6 (44.7)
	3KUR:A	716-791	544-616	32.9 (45.6)
	3KTP:A	716-791	544-616	32.9 (45.6)

a. PDB ID and chain identifier. b. in percentage
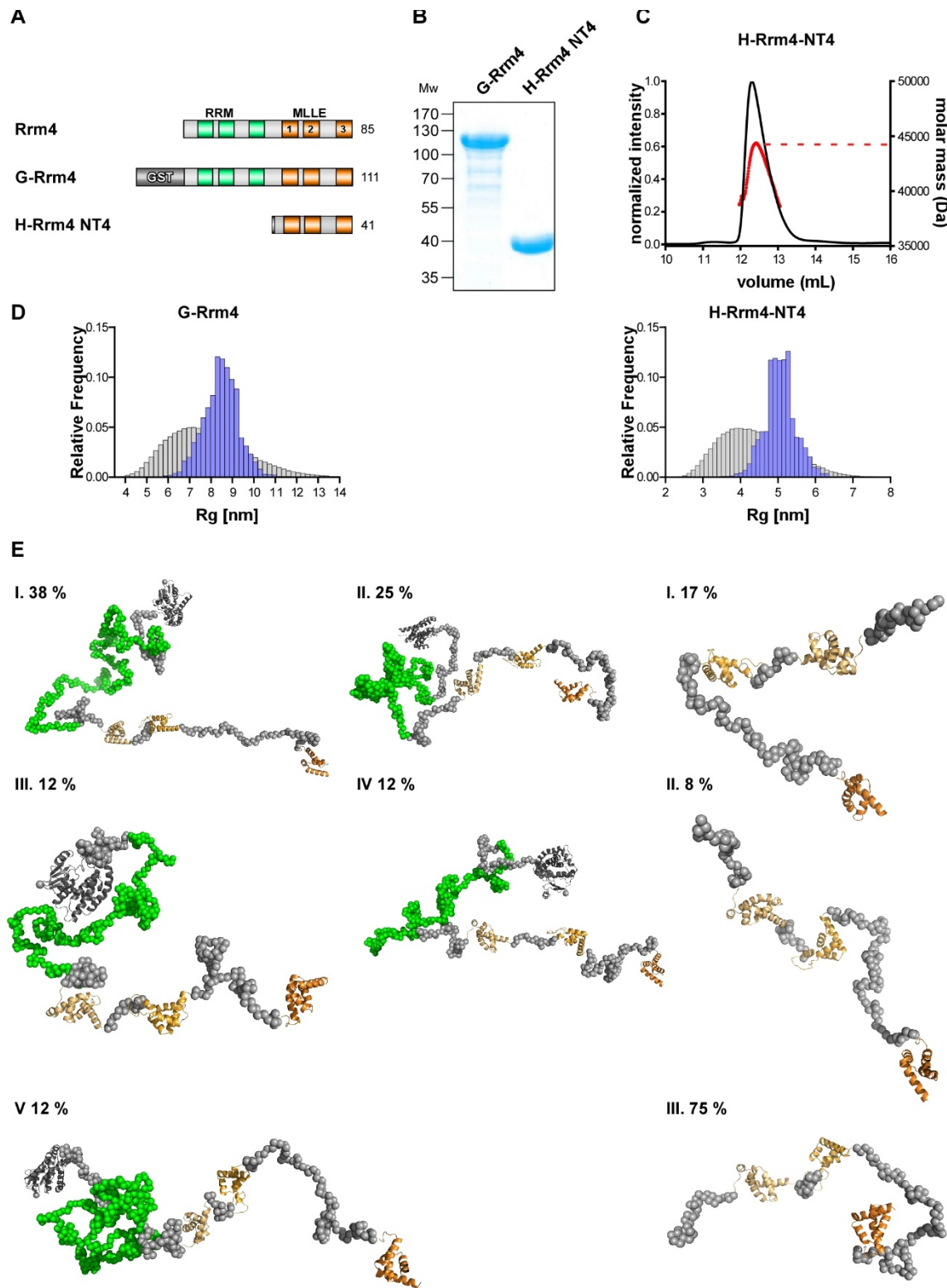
B
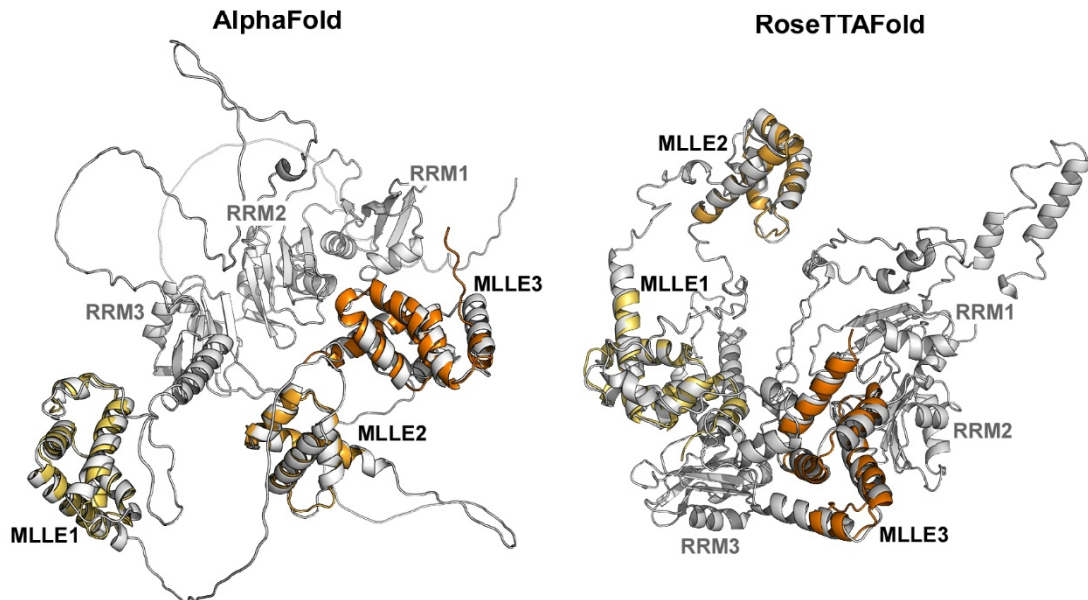
1026

1027 **Figure EV1. The presence of three MLLEs is verified by additional modelling predictions.**

1028 (**A**) Compilation of MLLE sequences used for modelling with the highest similarity of MLLE1-
1029 3[Rrm4]. (**B**) Structural models obtained with TopModel overlaid to Rrm4 full-length models
1030 obtained with the recently available tools as indicated. Natural alignments between
1031 corresponding MLLE domains have an RMSD < 2Å, mutually confirming the quality of the
1032 independently modelled structures. The differences in the relative domain arrangements in both
1033 full-length models and the disordered regions in between the domains suggest a high mobility
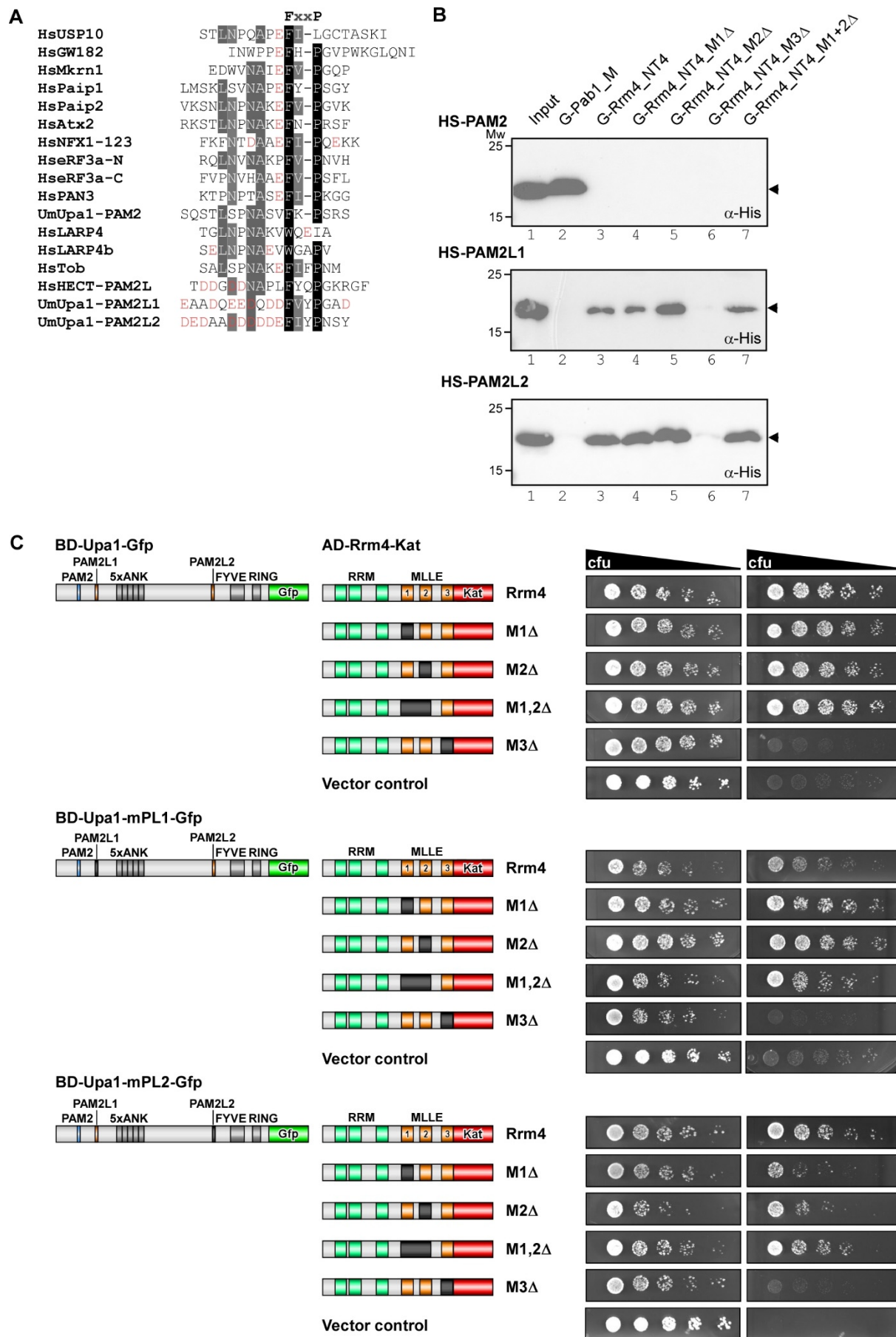1034 within Rrm4.

Devan, Schott-Verdugo *et al.*

Figure EV2. The three MLLEs of Rrm4 are located in a flexible C-terminal region.

(**A**) Schematic representation of protein variants drawn to scale (molecular weight in kilo Dalton indicated next to protein bar) using the following coloring: dark green, RNA recognition motif (RRM); orange, MLLE^Rrm4 domains; (**B**) SDS PAGE analysis of purified G-Rrm4, H-Rrm4-NT4 used in crystallography and SAXS measurement. (**C**) MALS-SEC analysis of H-Rrm4-NT4. Graph shows the elution profile. Dotted line in red indicate the apparent molecular
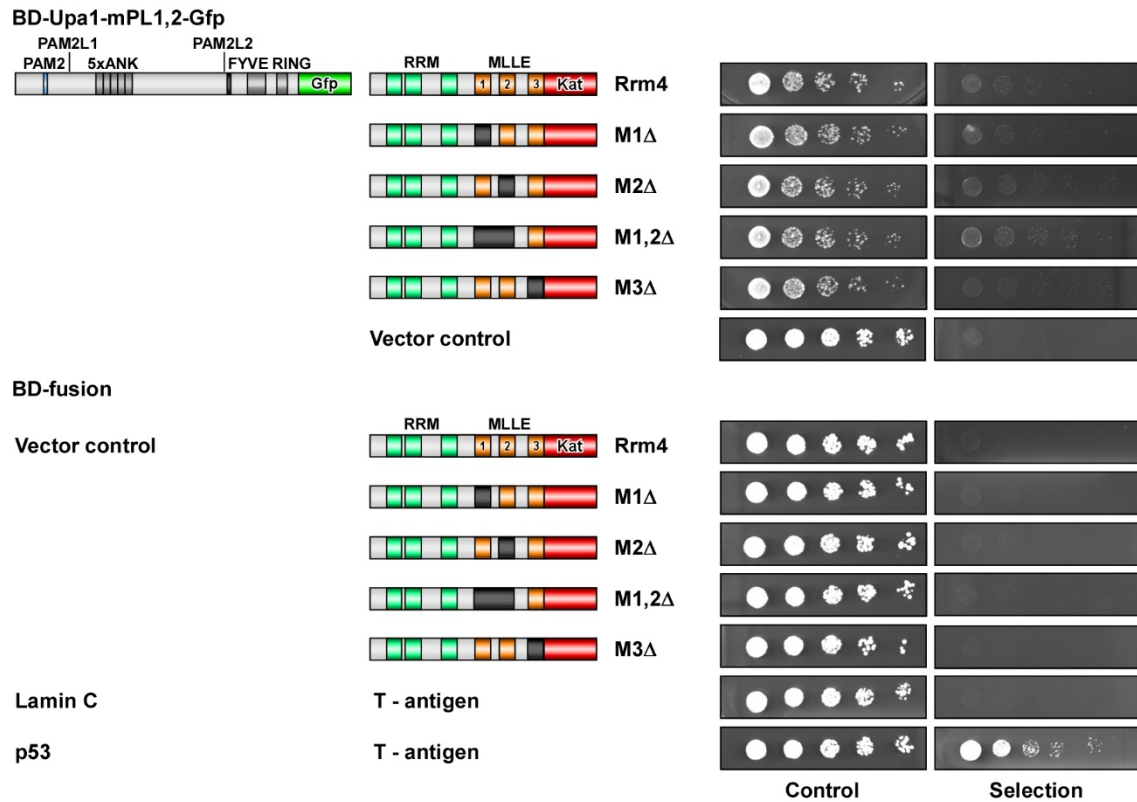
1042 weight as observed in the light scattering. (**D**) R_g distribution calculated by EOM pool is shown
1043 in grey bars and the selected models in blue bars *left* GST_Rrm4 *right* H-Rrm4NT4 (**E**) *Left*
1044 Selected models of the EOM analysis for GST-Rrm4. The MLLE subdomains and the GST are
1045 shown in cartoon representation (MLLE1 in light orange, MLLE2 in orange, MLLE 3 in dark
1046 orange) and the missing amino acids as grey spheres. **I:** The model has a R_g of 8.94 nm, a D_{max}
1047 of 29.22 nm with a volume fraction of~0.38. **II:** The model has a R_g of 8.75 nm, a D_{max} of 23.99
1048 with a volume fraction of~0.25. **III:** The model has a R_g of 7.74 nm, a D_{max} of 25.90 with a
1049 volume fraction of~0.12. **IV:** The model has a R_g of 8.33 nm, a D_{max} of 28.79 with a volume
1050 fraction of~0.12. **V:** The model has a R_g of 9.14 nm, a D_{max} of 33.73 with a volume fraction
1051 of~0.12. *Right* Selected models of the EOM analysis for H-Rrm4NT4. The MLLE subdomains
1052 are shown in cartoon representation (MLLE1 in light orange, MLLE2 in orange, MLLE3 in
1053 dark orange) and the missing amino acids as grey spheres. **I:** The model has a R_g of 5.12 nm,
1054 a D_{max} of 15.56 with a volume fraction of~0.17. **II:** The model has a R_g of 5.90 nm, a D_{max} of
1055 18.73 nm with a volume fraction of~0.08. **III:** The model has a R_g of 5.10 nm, a D_{max} of 16.43
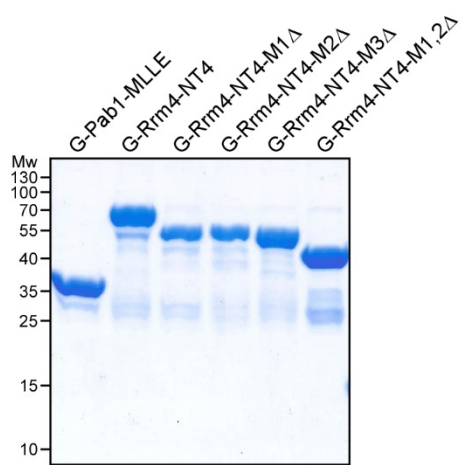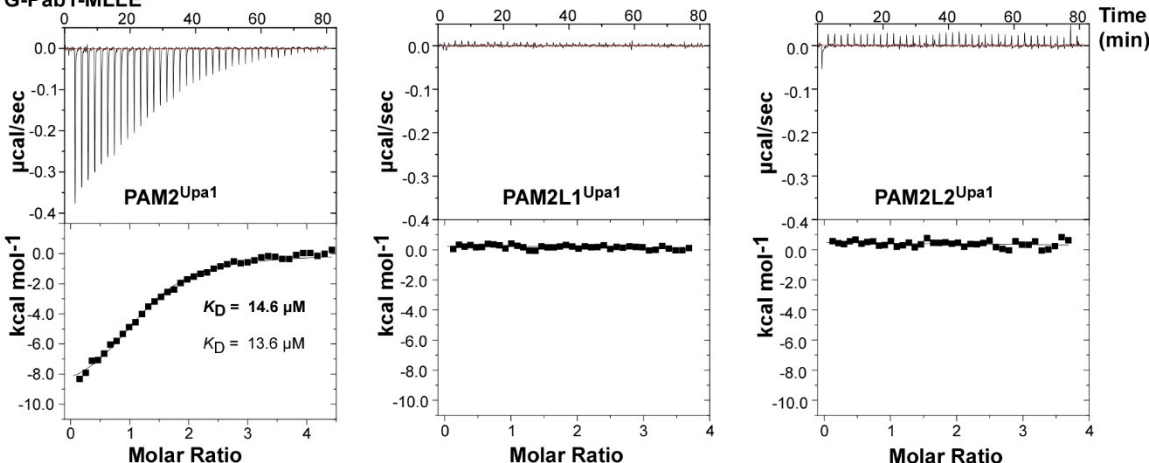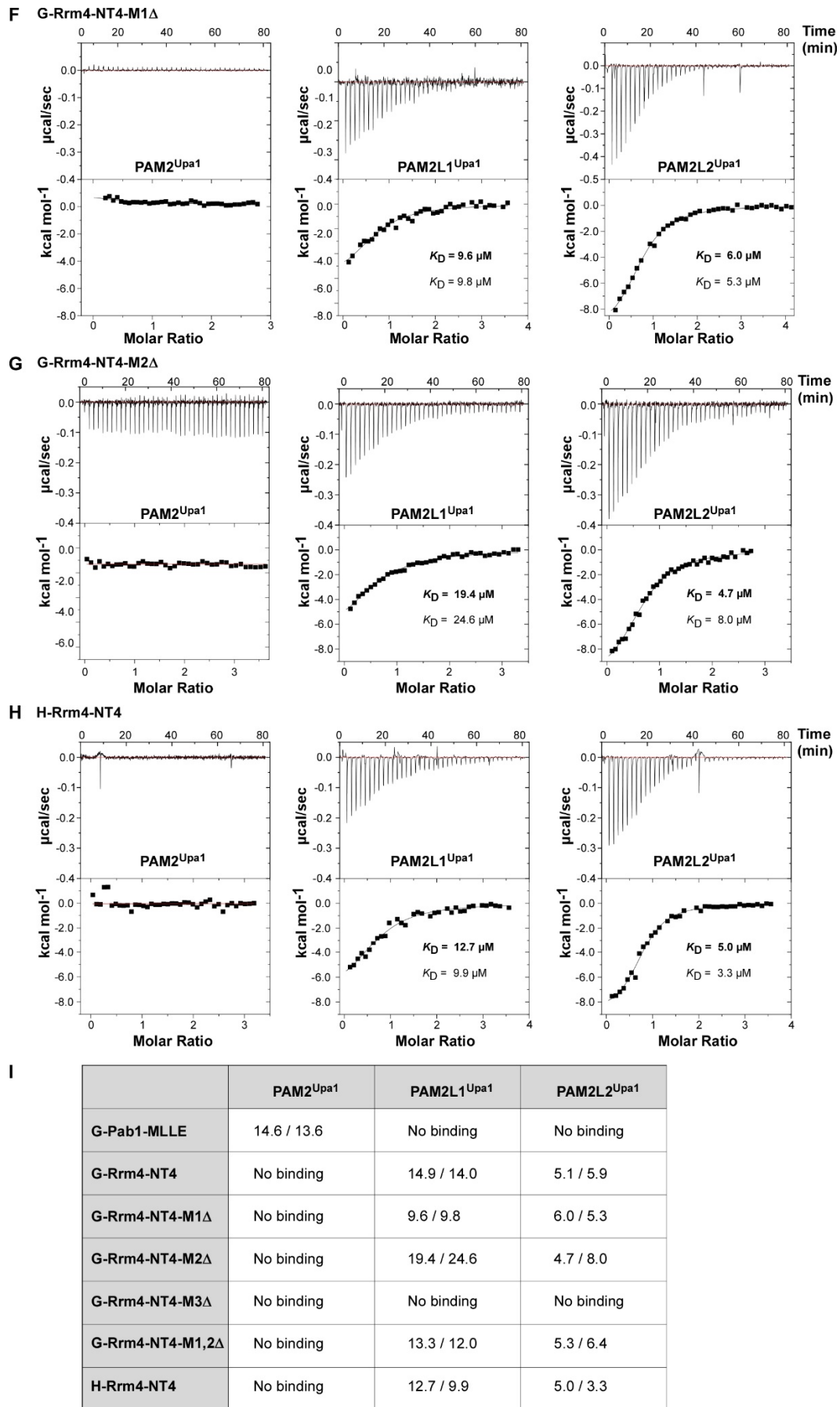1056 nm with a volume fraction of~0.75.
1057

1058
1059   Continued on next page

Continued on next page

F G-Rrm4-NT4-M1Δ

G G-Rrm4-NT4-M2Δ

H H-Rrm4-NT4

I

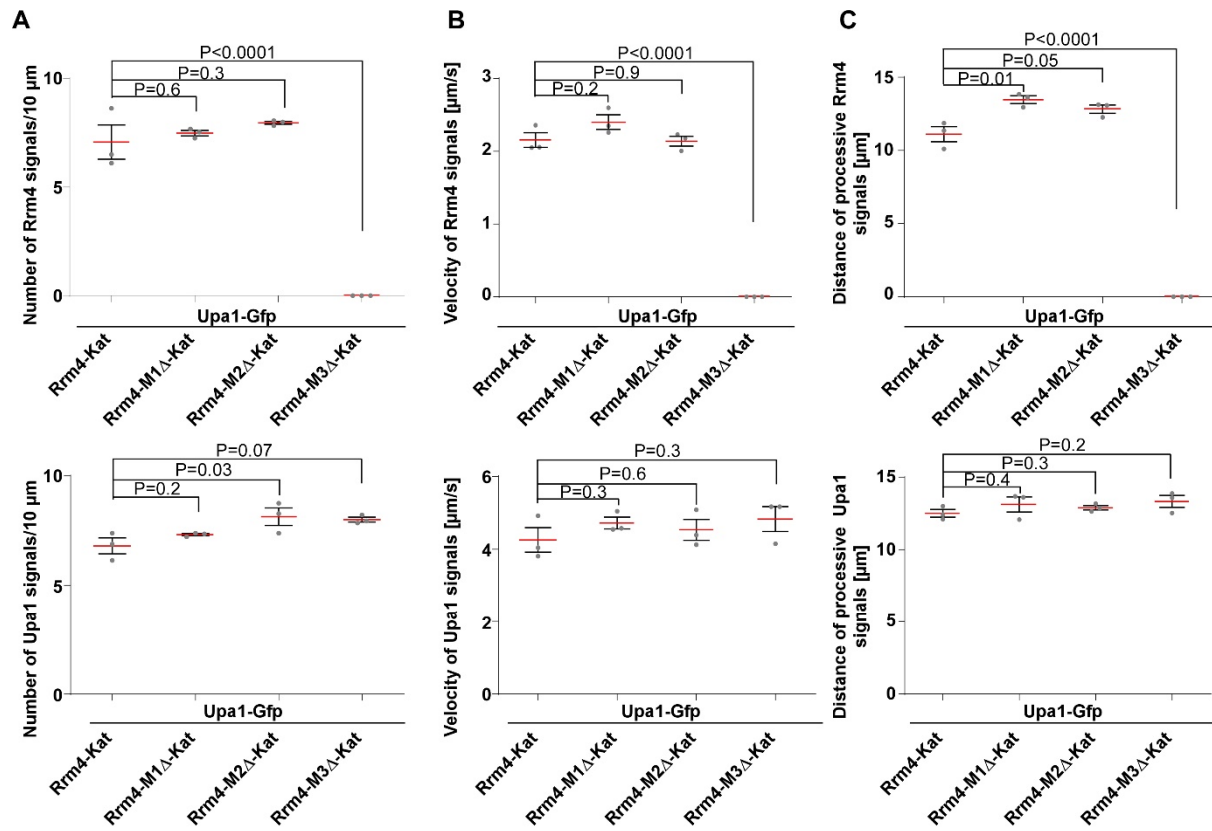|	PAM2^{Upa1}	PAM2L1^{Upa1}	PAM2L2^{Upa1}
G-Pab1-MLLE	14.6 / 13.6	No binding	No binding
G-Rrm4-NT4	No binding	14.9 / 14.0	5.1 / 5.9
G-Rrm4-NT4-M1Δ	No binding	9.6 / 9.8	6.0 / 5.3
G-Rrm4-NT4-M2Δ	No binding	19.4 / 24.6	4.7 / 8.0
G-Rrm4-NT4-M3Δ	No binding	No binding	No binding
G-Rrm4-NT4-M1,2Δ	No binding	13.3 / 12.0	5.3 / 6.4
H-Rrm4-NT4	No binding	12.7 / 9.9	5.0 / 3.3

1062

48

Devan, Schott-Verdugo *et al.*

Figure EV3. MLLE1 ^{Rrm4} , -2^{Rrm4} are not essential for PAM2L1^{Upa1} and -L2 ^{Upa1} binding.

(**A**) Comparison of PAM2 sequences found in Upa1 (UniprotKB ID A0A0D1E015) with those of human proteins, such as Usp10 (Q14694), GW182 Q9HCJ0), Mkrn1 (Q9UHC7), Paip1 (Q9H074), Paip2 (Q9BPZ3), Atx2 (-Q99700), NFX (Q12986), eRF3 (P15170), PAN3 (Q58A45), LARP4 (Q71RC2), LARP4b (Q92615), Tob (P50616), HECT (O95071), Asp and Glu are indicated in red stressing the highly negative charges in PAM2L sequences. (**B**) Western blot analysis of GST co-purification experiments with components expressed in *E. coli*: N-terminal Hexa-Histidine-SUMO-tagged PAM2 variants were pulled down by N-terminal GST fused MLLE variants of Rrm4 and Pab1. Experiment was performed with the soluble fraction of *E. coli* cell lysate to demonstrate specific binding. Results were analysed with αHis immunoblotting (**C**) Yeast two-hybrid analyses with schematic representation of protein variants tested on the left. Cultures were serially diluted 1:5 (decreasing colony-forming units, cfu) and spotted on respective selection plates controlling transformation and assaying reporter gene expression (see Materials and methods). (**D**) SDS-PAGE analysis of purified GST-MLLE variants used in ITC experiments (**E-H**) Representative isothermal titration calorimetry (ITC) binding curves of MLLE domains. Experiments were performed using GST or hexa-histidine-tagged MLLE variants and synthetic PAM2 peptide variants. K_D values of two independent measurements are given (values corresponding to the indicated data are given in bold). (**I**) Summary of ITC results shown in Fig. 3 and Fig. EV3. K_D values are given in μM.

A

B

C

D

upa1	rrm4	Phenotype	Endosomal shuttling of Rrm4	Microtuble binding of Rrm4
wt	wt	wt	wt	wt
wt	rrm4Δ	bipolar	not applicable	not applicable
wt	m1Δ	wt	wt	wt
wt	m2Δ	wt	wt	wt
wt	m3Δ	bipolar	abolished	not applicable
wt	m1,2Δ	wt	wt	wt
pl1,2m	wt	bipolar	aberrant	strong
upa1Δ	wt	bipolar	aberrant	strong
pl1,2m	m1,2Δ	bipolar	aberrant	strong
pl1m	wt	wt	wt	weak
pl2m	wt	wt	wt	medium
pl1m	m1,2Δ	wt	wt	weak
pl2m	m1,2Δ	wt	wt	strong
pl2m	m1Δ	wt	wt	medium
pl2m	m2Δ	wt	wt	strong

1083

1084 **Figure EV4. Deletion of MLLE3^{Rrm4} abolishes endosomal movement of Rrm4**

50

1085   (**A-C**) Quantification of processive Rrm4-Kat (top) and Upa1-Gfp signals (bottom; (**A**)),
1086   velocity of fluorescent Rrm4-Kat (top) and Upa1-Gfp signals (bottom; (**B**)) and the travelled
1087   distance of processive Rrm4-Kat (top) and Upa1-Gfp signals (bottom; (**C**); per 10 µm of hyphal
1088   length; only particles with a processive movement of > 5 µm were conducted; data points
1089   representing mean from n =3 independent experiments, with mean of means, red line and SEM;
1090   unpaired two-tailed Student's t-test ($\alpha<0.05$), for each experiment at least 25 hyphae were
1091   analysed per strain). (**D**) Summary of the *in vivo* analysis is shown in Fig. 4,5 and Fig. EV5A-
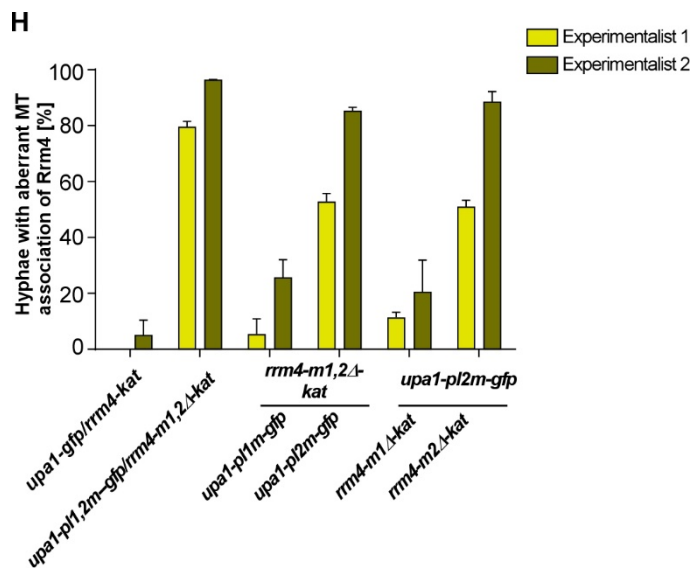1092   C.

H
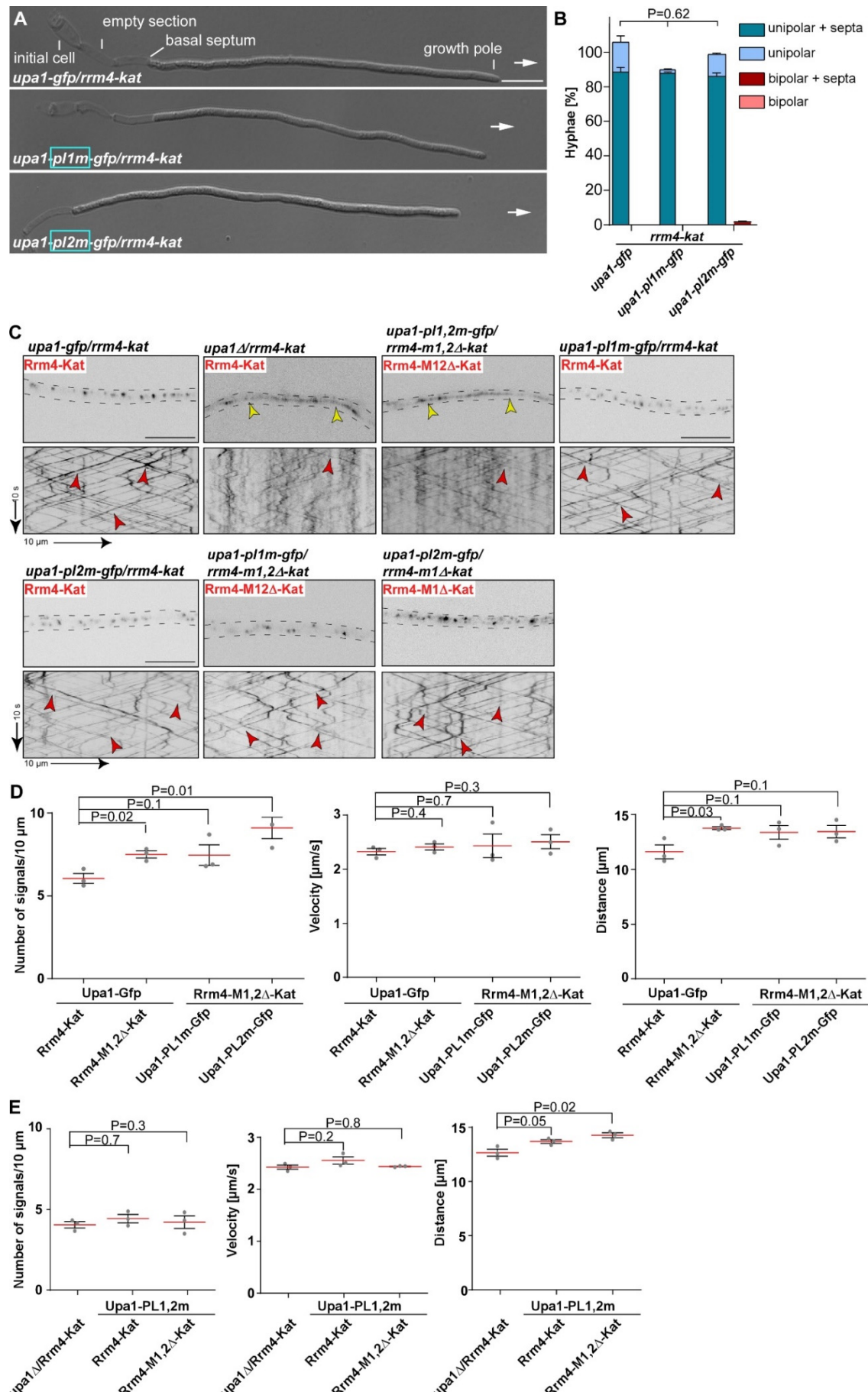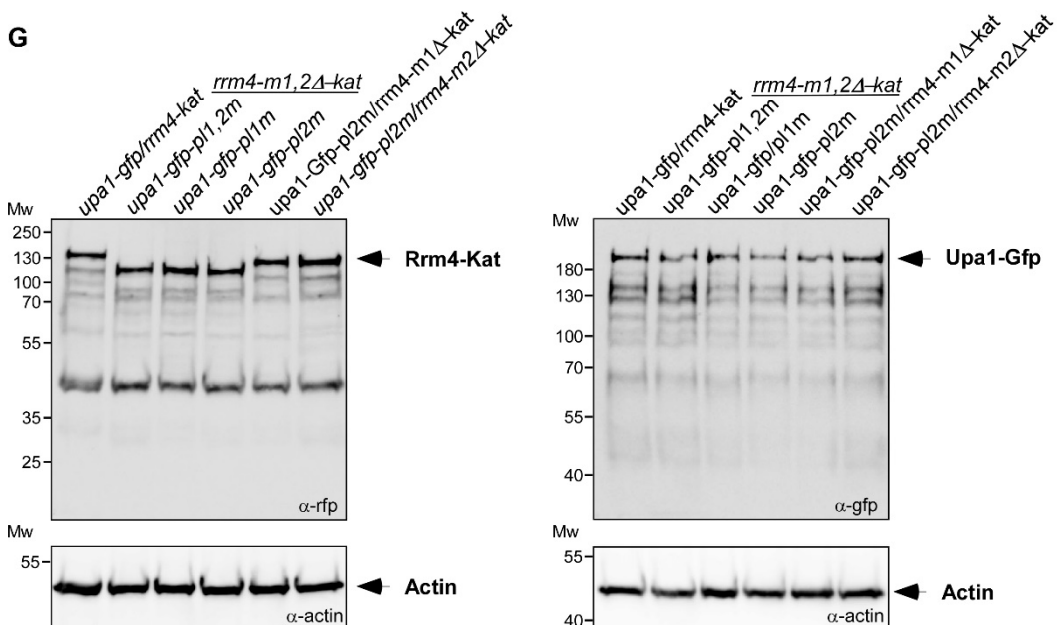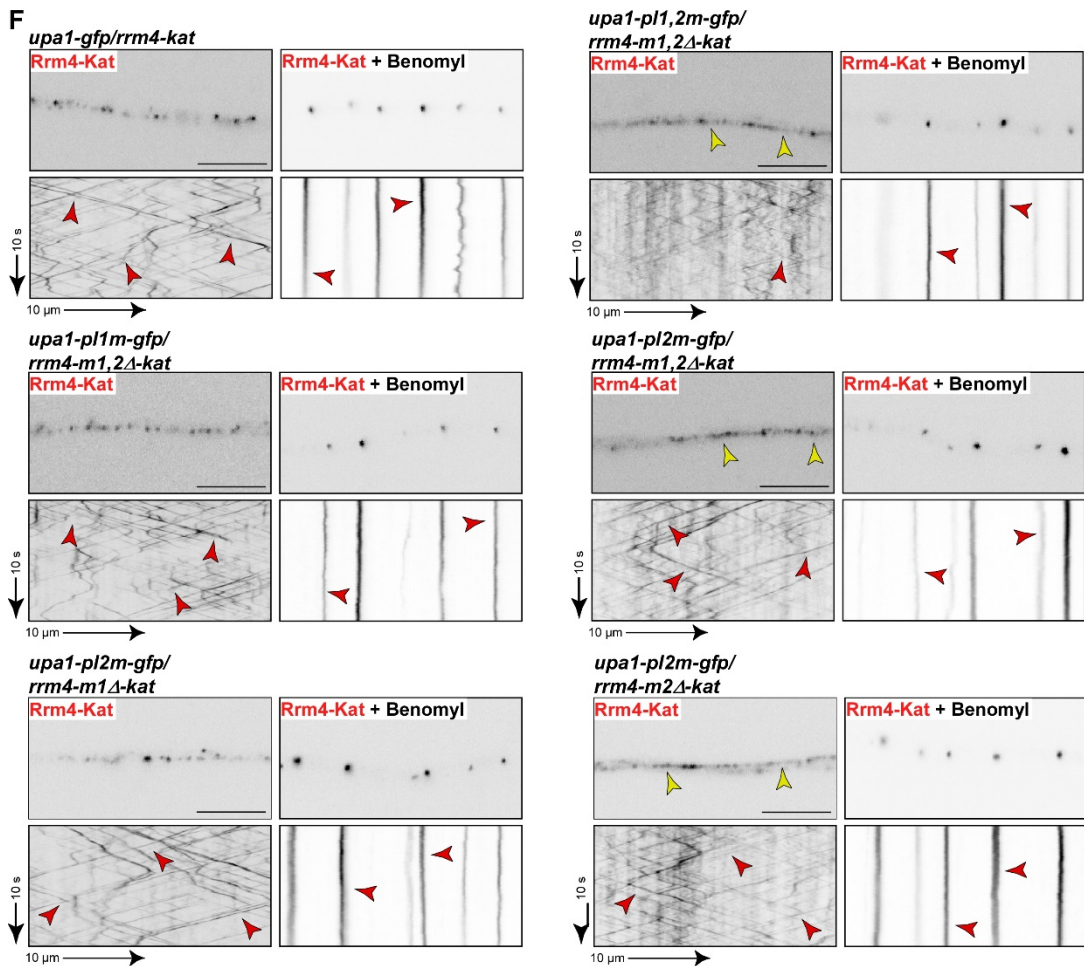
Figure EV5. Deletion of MLLE1^{Rrm4} and -2 cause aberrant staining of microtubules

(**A**) Growth of AB33 derivatives in their hyphal form (6 h.p.i.; size bar 10 μm). Growth direction is marked by arrows. (**B**) Quantification of hyphal growth of AB33 derivatives shown in panel A (6 h.p.i.): unipolarity, bipolarity and basal septum formation were quantified (error bars, SEM.; n = 3 independent experiments, > 100 hyphae were analysed per strain; For statistical evaluation, the percentage of uni- and bipolarity was investigated by using unpaired two-tailed Student's t-test ($\alpha<0.05$). (**C**) Micrograph and Kymograph of AB33 hyphae derivates (6 h.p.i.) expressing red and green fluorescent proteins as indicated. Fluorescence signals were detected simultaneously using dual-view technology (arrow length on the left and bottom indicates time and distance, respectively). Processive co-localising signals are marked by red arrowheads. Aberrant microtubule staining is indicated by a yellow arrowhead. (**D-E**) Quantification of processive Rrm4-Kat signals (left), velocity of fluorescent Rrm4-Kat (middle) and the travelled distance of processive Rrm4-Kat signals (right) related to figure 5 C and EV5C, respectively (per 10 μm of hyphal length; only particles with a processive movement of > 5 μm were conducted; data points representing mean from n =3 independent experiments, with mean of means, red line and SEM; unpaired two-tailed Student's t-test ($\alpha<0.05$), for each experiment at least 25 hyphae were analysed per strain). (**F**) Benomyl treatment is shown in micrograph and kymograph of AB33 hyphae derivates (6 h.p.i.) expressing red and green fluorescent proteins. Processive signals, as well as static signals, post benomyl treatment are marked by red arrowheads. Aberrant microtubule staining is indicated by a yellow arrowhead. (**G**) Western blot analysis of the expression levels of Rrm4 and Upa1 variants 6 h.p.i. of hyphal growth. Rrm4 and Upa1 variants were detected via mKate2 and Gfp, respectively. Actin was detected as loading control. Bands representing full-length proteins are marked with arrows. (**H**) Evaluation of the most important strains showing aberrant microtubule staining analysed by two experimentalists (we used the data obtained by the more experienced microscopist in Fig. 5D; see Materials and methods).